

Tuning Frictional Properties of Kirigami Altered Graphene Sheets using Molecular Dynamics and Machine Learning

Designing a Negative Friction Coefficient

Mikkel Metzsch Jensen



Thesis submitted for the degree of
Master in Computational Science: Materials Science
60 credits

Department of Physics
Faculty of mathematics and natural sciences

UNIVERSITY OF OSLO

Spring 2023

Tuning Frictional Properties of Kirigami Altered Graphene Sheets using Molecular Dynamics and Machine Learning

Designing a Negative Friction Coefficient

Mikkel Metzsch Jensen



© 2023 Mikkel Metzsch Jensen

Tuning Frictional Properties of Kirigami Altered Graphene Sheets using Molecular Dynamics and Machine Learning

<http://www.duo.uio.no/>

Printed: Reprocentralen, University of Oslo

Abstract

Abstract.

Acknowledgments

Acknowledgments.

List of Symbols

F_N Normal force (normal load)

Acronyms

AFM atomic force microscope. 21, 22, 23, 25

FFM friction force microscopes. 21, 22, 23, 25

FK Frenkel-Kontorova. 11, 16, 17, 18, 19, 20, 23, 24, 25

FKT Frenkel–Kontorova–Tomlinson. 11, 20

GS ground state. 17, 18

MD molecular dynamics. 2, 3, 10, 11, 12, 14, 23, 24, 25

ML machine learning. 2, 3

PT Prandtl–Tomlinson. 11, 16, 17, 19, 20, 22

SFA Surface force apparatus. 22, 23

SFM scanning force microscopies. 21

SPM scanning probe microscopy. 21

Contents

1	Introduction	1
1.1	Motivation	1
1.2	Goals	3
1.3	Contributions	3
1.4	Thesis structure	3
I	Background Theory	5
2	Friction	7
2.1	Friction across scales	7
2.2	Macroscale	7
2.2.1	Amontons' law	8
2.3	Microscopic scale	9
2.3.1	Asperity theories	9
2.4	Nanoscale — Atomic scale	10
2.4.1	Prandtl–Tomlinson	11
2.4.1.1	Thermal activation	12
2.4.1.2	Sliding speed	14
2.4.1.3	Tip mass	15
2.4.1.4	Friction Regimes: Smooth Sliding, Single Slip, and Multiple Slip	15
2.4.2	Frenkel-Kontorova	16
2.4.2.1	Commensurability	17
2.4.2.2	Velocity resonance	19
2.4.3	Frenkel-Kontorova-Tomlinson	20
2.4.4	Shortcomings of atomic models	21
2.4.5	Experimental procedures	21
2.4.5.1	Scanning Probe Microscopy	21
2.4.5.2	Surface Force Apparatus	22
2.5	Expected frictional properties of graphene	22
2.6	Research questions	27
3	Molecular Dynamics	29
3.1	Potentials	29
3.1.1	General formulation of potentials (?)	29
3.1.2	Lennard Jones	29
3.1.3	Stillinger weber	30
3.1.4	Tersoff	31
3.2	Integration	32
3.2.1	Velocity Verlet	33
3.3	Thermostats	33
3.3.1	Langevin thermostat	34
3.3.2	Implementing Langevin	36
3.4	MD limitations (?)	36

3.5 LAMMPS	36
II Simulations	37
Appendices	39
Appendix A	41
Appendix B	43
Appendix C	45

Chapter 1

Introduction

Structure of Motivation section:

1. Introduce and motivate friction broadly.
2. Motives for friction control using a grasping robot as example.
3. Analog to gecko feet where adhesive properties are turned on and off.
4. Interest in origin of friction through nanoscale studies which further motivates the use of MD.
5. Intro to metamaterials and the use of kirigami designs,
6. How to optimize kirigami designs with reference to Hanakata and motivating the use of ML.
7. Out-of-plane buckling motivates the use of kirigami for frictional properties.

Does some of the latter paragraphs belong to the approach section?

1.1 Motivation

Friction is a fundamental force that takes part in most of all interactions with physical matter. Even though the everyday person might not be familiar with the term *friction* we recognize it as the inherent resistance to sliding motion. Some surfaces appear slippery and some rough, and we know intuitively that sliding down a snow covered hill is much more exciting than its grassy counterpart. Without friction, it would not be possible to walk across a flat surface, lean against the wall without falling over or secure an object by the use of nails or screws [p. 5] [1]. It is probably safe to say that the concept of friction is integrated in our everyday life to such an extent that most people take it for granted. However, the efforts to control friction dates back to the early civilization (3500 B.C.) with the use of the wheel and lubricants to reduce friction in translational motion [2]. Today, friction is considered a part of the wider field *tribology* derived from the Greek word *Tribos* meaning “rubbing” and includes the science of friction, wear and lubrication [2]. The most compelling motivation to study tribology is ultimately to gain full control of friction and wear for various technical applications. Especially, reducing friction is of great interest as this has tremendous advantages for energy efficiency. It has been reported that tribological problems have a significant potential for economic and environmental improvements [3]:

“On global scale, these savings would amount to 1.4% of the GDP annually and 8.7% of the total energy consumption in the long term.” [4].

On the other hand, the reduction of friction is not the only sensible application for tribological studies. Controlling frictional properties, besides minimization, might be of interest in the development of a grasping robot where a finetuned object handling is required. While achieving a certain “constant” friction response is readily obtained through appropriate material choices during manufacturing, we are yet to unlock the capabilities to alter friction dynamically on the go. One example from nature inspiring us to think along these lines are the gecko feet. More precisely, the Tokay gecko has received a lot of attention in scientific studies aiming to unravel the underlying

mechanism of its “toggable” adhesion properties. Although geckos are able to produce large adhesive forces, they retain the ability to remove their feet from an attachment surface at will [5]. This makes the gecko able to achieve a high adhesion on the feet when climbing a vertical surface while lifting it for the next step remains relatively effortless. For a grasping robot we might consider an analog frictional concept of a surface material that can change from slippery to rough on demand depending on specific tasks.

In the recent years an increasing amount of interest has gone into the studies of the microscopic origin of friction, due to the increased possibilities in surface preparation and the development of nanoscale experimental methods. Nano-friction is also of great concern for the field of nano-machining where the frictional properties between the tool and the workpiece dictates machining characteristics [3]. With concurrent progress in computational power and development of Molecular Dynamics (MD), numerical investigations serve as an extremely useful tool for getting insight into the nanoscale mechanics associated with friction. This simulation based approach can be considered as a “numerical experiment” enabling us to create and probe a variety of high complexity systems which are still out of reach for modern experimental methods.

In materials science such MD-based numerical studies have been used to explore the concept of so-called *metamaterials* where material compositions are designed meticulously to enhance certain physical properties [6][7][8][9][10][11]. This is often achieved either by intertwining different material types or removing certain regions completely. In recent papers by Hanakata et al. [6](2018) [7](2020) numerical studies have showcased that mechanical properties of a graphene sheet, in this case yield stress and yield strain, can be altered through the introduction of so-called *kirigami* inspired cuts into the sheet. Kirigami is a variation of origami where the paper is cut additionally to being folded. While these methods originate as an art form, aiming to produce various artistic objects, they have proven to be applicable in a wide range of fields such as optics, physics, biology, chemistry and engineering [12]. Various forms of stimuli enable direct 2D to 3D transformations through folding, bending, and twisting of microstructures. While original human designs have contributed to specific scientific applications in the past, the future of this field is highly driven by the question of how to generate new designs optimized for certain physical properties. However, the complexity of such systems and the associated design space makes for seemingly intractable problems ruling out analytic solutions.

Earlier architecture design approaches such as bioinspiration, looking at gecko feet for instance, and Edisonian, based on trial and error, generally rely on prior knowledge and an experienced designer [9]. While the Edisonian approach is certainly more feasible through numerical studies than real world experiments, the number of combinations in the design space rather quickly becomes too large for a systematic search, even when considering the simulation time on modern day hardware. However, this computational time constraint can be relaxed by the use of machine learning (ML) which have proven successful in the establishment of a mapping from the design space to physical properties of interest. This gives rise to two new styles of design approaches: One, by utilizing the prediction from a trained network we can skip the MD simulations all together resulting in an *accelerated search* of designs. This can be further improved by guiding the search accordingly to the most promising candidates, as for instance done with the *genetic algorithm* which suggest new designs based on mutation and crossing of the best candidates so far. Another, even more sophisticated approach, is through generative methods such as *Generative Adversarial Networks* (GAN). By working with a so-called *encoder-decoder* network structure, one can build a model that reverses the prediction process. That is, the model predicts a design from a set of physical target properties. In the papers by Hanakata et al. both the *accelerated search* and the *inverse design* approach was proven successful to create novel metamaterial kirigami designs with the graphene sheet.

Hanakata et al. attributes the variety in yield properties to the non-linear effects arising from the out-of-plane buckling of the sheet. Since it is generally accepted that the surface roughness is of great importance for frictional properties it can be hypothesized that the kirigami cut and stretch procedure can also be exploited for the design of frictional metamaterials. For certain designs we might hope to find a relationship between stretching of the sheet and frictional properties. If significant, this could give rise to a variability of the friction response beyond manufacturing material choice. For instance, the grasping robot might apply such a material as artificial skin for which stretching or relaxing of the surface could result in a changeable friction strength; Slippery and smooth when in contact with people and rough and firmly gripping when moving heavy objects. In addition, a possible coupling between stretch and the normal load through a nanomachine design would allow for an altered friction coefficient. This invites the idea of non-linear friction coefficients which might in theory also take on negative values given the right response from stretching. The latter would constitute an extremely rare property. This has (**only?**) been reported indirectly for bulk graphite by Deng et al. [13] where the friction kept increasing during the unloading phase. **Check for other cases and what I can really say here.**

To the best of our knowledge, kirigami has not yet been implemented to alter the frictional properties of a nanoscale system. In a recent paper by Liefferink et al. [14](2021) it is reported that macroscale kirigami can be used to dynamically control the macroscale roughness of a surface through stretching which was used to change the frictional coefficient by more than one order of magnitude. This supports the idea that kirigami designs can in fact be used to alter friction, but we believe that taking this concept to the nanoscale regime would involve a different set of underlying mechanisms and thus contribute to new insight in this field.

1.2 Goals

In this thesis we investigate the possibility to alter and control the frictional properties of a graphene sheet through application of kirigami inspired cuts and stretching of the sheet. With the use of MD simulations we evaluate the friction properties under different physical conditions in order to get insight into the prospects of this field. By evaluating variations of two kirigami inspired patterns and a series of random walk generated patterns we create a dataset containing information of the frictional properties associated with each design under different load and stretch conditions. We apply ML to the dataset and use an accelerated search approach to optimize for different properties of interest. The subtask of the thesis are presented more comprehensively in the following.

1. Define a sheet indexing that allows for a unique mapping of patterns between a hexagonal graphene lattice representation to a matrix representation suited for numerical analysis.
2. Design a MD simulation procedure to evaluate the frictional properties of a given graphene sheet under specified physical conditions such as load, stretch, temperature etc.
3. Find and implement suitable kirigami patterns which exhibit out-of-plane buckling under tensile load. This includes the creation of a framework for creating variations within each pattern class. Additionally create a procedure for generating different styles of random walk patterns.
4. Perform a pilot study of a representative subset of patterns in order to determine appropriate simulation parameters to use for the further study along with an analysis of the frictional properties shown in the subset.
5. Create a dataset consisting of the chosen kirigami variations and random walk patterns and analyse data trends.
6. Train a neural network to map from the design space to physical properties such as mean friction, maximum friction, contact area etc. and evaluate the performance.
7. Perform an accelerated search optimizing for interesting frictional properties using the ML model. This should be done both through the pattern generation procedures and by following a genetic algorithm approach.
8. Use the most promising candidates from the accelerated search to investigate the prospects of creating a nanomachine setup which exhibits a negative friction coefficient.
9. Study certain designs of interest with the scope of revealing underlying mechanism. This includes simple correlation analysis but also a visualization of feature and gradient maps of the ML network.

Is the list of subtask too specific? Some of the details here might be better suited for the thesis structure section.

1.3 Contributions

What did I actually achieve

1.4 Thesis structure

How is the thesis structured.

Part I

Background Theory

Chapter 2

Friction

Friction plays a central role for the topic of this thesis being the key concept that we want to explore through the design of nanostructures. In this chapter we review the relevant theoretical understanding and highlight the derived expectations for our study.

Friction is a part of the wider field tribology which includes the study of friction, wear and lubrication between two surfaces in relative motion [1, p. 1]. In this thesis we will only concern ourselves with so-called wearless dry friction. That is, without any use of lubrication and without any resulting wear of the contacting surfaces.

2.1 Friction across scales

Tribological systems take place across a broad range of time and length scales, ranging from geological stratum layers involved in earthquakes [3] to atomistic processes, as in the gliding motion of a nanocluster or a nanomotor [15]. This vast difference in scale gives rises to different frictional mechanism being dominating. On a macro scale the system is usually subject to a relatively high load and sliding speed leading to a high contact stress and wear. On the other hand, the micro-/nanoscale regime occupies the opposite domain operating under relatively small load and sliding speed with negligible wear [3] [2, p. 5]. While macroscale friction is often reduced into a few variables such as load, material type, sliding speed and surface roughness, it is clear that the micro-/nanoscale friction cannot be generalized under such a simple representation. On the micro-/nanoscale the tribological properties are dominated by surface properties which will yield a more complex behaviour of said variables and introduce an additional sensitivity to variables such as temperature, humidity and even sliding history. The works of Bhushan and Kulkarni [16] showed that the friction coefficient decreased with scale even though the materials used was unchanged. This reveals an intrinsic relationship between friction and scale as the contact condition is altered.

The phenomenological descriptions of macroscale friction cannot yet be derived from the fundamental atomic principles, and bridging the gap between different length scales in tribological systems remains an open challenge [15]. Hence, the following sections will be organized into macroscale (Sec. 2.2), microscale (Sec. 2.3) and nanoscale (Sec. 2.4) representing the theoretical understanding governing each scale regime. Realising that the field of tribology across all scales is a vastly broad and intricate topic, we will aim to introduce only the essential findings for each scale, while keeping a main focus on necessary theoretical background associated to the understanding of our system of interest which takes place at the lowest scale.

2.2 Macroscale

Our working definition of the *macroscale* is everything on the scale of visible objects. This is usually denoted to the size of millimeters 10^{-3} m and above. Most importantly, we want to make a distinction to the microscale, where the prefix indicates the size of micrometers m^{-6} . Hence, we essentially consider everything larger than *micro* to belong to the macroscale¹.

¹The width of a human hair is often used as a reference for the limit of human perception. Since the width of a human hair is on the length scale 10^{-5} to 10^{-4} m we find this limit aligns rather well with the defined transition from macro- to microscale.

2.2.1 Amontons' law

In order to start and keep a solid block moving against a solid surface we must overcome certain frictional forces F_{fric} [1]. The static friction force F_s corresponds to the minimum tangential force required to initiate the sliding while the kinetic friction force F_k corresponds to the tangential force needed to sustain such a sliding at steady speed. The work of Leonardo da Vinci (1452–1519), Guillaume Amontons (1663–705) and Charles de Coulomb (1736–1806) all contributed to the empirical law, commonly known as *Amontons' law*, which serves as a common base for macroscale friction. Amontons' law states that the frictional forces is entirely independent of contact area and sliding velocity. Instead, it relies only on the normal force F_N , acting perpendicular to the surface, and the material specific friction coefficient μ as

$$F_{\text{fric}} = \mu F_N. \quad (2.1)$$

Notice that the term *Normal force* is often used interchangeably with *load* and *normal load* although the latter two terms refer to the applied force, “pushing” the object into the surface, and the first is the reaction force acting from the surface on the object. In equilibrium, these forces are equal in magnitude and hence we will not make a distinction between these terms. On the same note, we point out that the frictional force is different from a conventional force which in the Newtonian definition acts on a body from the outside and make it accelerate [17]. Rather than being an independent external force the friction force is an internal *reaction* force opposing the externally applied “sliding” force.

The friction coefficient μ is typically different for the cases of static (μ_s) and kinetic (μ_k) friction, usually both with values lower than one and $\mu_s \geq \mu_k$ in all cases [1, p. 6]. The friction coefficient is taken to be a constant defined by either [17]

$$\mu_1 = \frac{F_{\text{fric}}}{F_N}, \quad (2.2a)$$

or

$$\mu_2 = \frac{dF_{\text{fric}}}{dF_N}. \quad (2.2b)$$

The first definition Eq. (2.2a) requires zero friction at zero load, i.e. $F_{\text{fric}} = 0$ at $F_N = 0$, while the second definition Eq. (2.2b) allows for a finite friction force at zero load as the coefficient is defined by the slope of the $F_{\text{fric}}-F_N$ -curve. The consequences of these definitions are illustrated in Fig. 2.1, for selected $F_{\text{fric}}-F_N$ -curves in Fig. 2.1a and corresponding friction coefficients in Fig. 2.1b and Fig. 2.1c. For adhesive contacts the friction force will not be zero under zero load (red curve: Linear + shift) which can be mitigated by adding an extra constant to Eq. (2.1) [17]. Using Eq. (2.2a) for adhesive contacts would make the friction coefficient diverge for decreasing load as illustrated in Fig. 2.1b. Thus, we find the second definition Eq. (2.2b) more robust and versatile. This also allows for a better interpretation of the friction coefficient in the hypothetical case where friction depends non-linearly on load (Purple curve in Fig. 2.1).

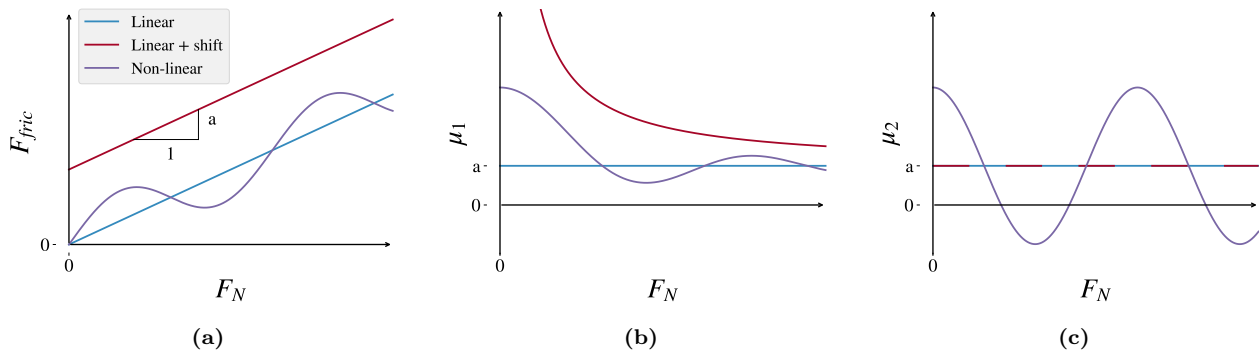


Figure 2.1: CAPTION

Although Amontons' law has been successful in its description of the majority of rubbing surfaces, involving both dry and lubricated, ductile and brittle and rough and smooth (as long as they are not adhesive) surfaces [17], it has its limitations. It is now known that Eq. (2.1) is not valid over a large range of loads and sliding velocities and that it completely breaks down for atomically smooth surfaces in strongly adhesive contact [17]. For instance, the independency of sliding velocity disappears at low velocities as thermal effects become important and for

high velocities due to inertial effects [1, pp. 5-6]. For the case of static friction, it was discovered to be dependent on the so-called contact history with increasing friction as the logarithm of time of stationary contact [18].

In cases where Amontons' law breaks down we might still use the conceptual definition of the friction coefficient as defined by (Eq. (2.2b)). Especially, in the context of achieving negative friction coefficients (in certain load ranges) we would refer to this definition, since Eq. (2.2a) would imply a truly unphysical situation of the frictional force acting in the same direction as the sliding motion. This would accelerate the object indefinitely².

Due to the empirical foundation of Amontons' law it does not provide any physical insight into the underlying mechanisms of friction. However, as we will later discuss in more detail, we can understand the overall phenomena of friction through statistical mechanics by the concept of *equipartition of energy* [15]. A system in equilibrium has its kinetic energy uniformly distributed among all its degrees of freedom. When a macroscale object is sliding in a given direction it is clearly not in equilibrium since one of its degrees of freedom carries considerable more kinetic energy. Thus, the system will have a tendency to transfer kinetic energy to the remaining degrees of freedom as heat which dissipates to the surroundings and making the object slow down if not continuously driven forward by an external energy source. Hence, we can understand the overall concept of friction simply as the tendency of going toward equilibrium energy equipartitioning among many interacting degrees of freedom [15]. From this point of view it is clear that friction is an inevitable part of contact physics, but even though friction cannot be removed altogether, we are still capable of manipulating it in useful ways.

The attentive reader might point out that we have already moved the discussion into the microscopic regime as *statistical mechanics* generally aim to explain macroscale behaviour by microscopic interactions. In fact, this highlights the necessity to consider smaller scales in order to achieve a more fundamental understanding of friction.

2.3 Microscopic scale

Going from a macro- to a microscale perspective, at a length scale on the order 10^{-6} m, it was realised that most surfaces are in fact rough [19]. The contact between two surfaces consists of numerous smaller contact points, so-called *asperities*, which form junctions due to contact pressure and adhesion as visualized in Fig. 2.2 [3]. In the macroscale perspective of Amonton's law we refer to time- and space-averaged values, i.e. the apparent contact area and the average sliding speed [17]. However, microscopically we find the real contact area to be much smaller than the apparent area [3], and the shearing motion of local microjunctions to happen at large fluctuations rather than as one synchronized movement throughout the surface.

It is generally accepted that friction is caused by two mechanisms: Mechanical friction and chemical friction [3]. The mechanical friction is the “plowing” of the surface by hard particles or said asperities with an energy loss attributed to deformations of the asperity. While plastic deformations, corresponding to wear, gives rise to an obvious attribution for the energy loss, elastic deformations are also sufficient in explaining energy loss due to phonon excitations. In fact the assumption of plastic deformations has been criticized as this is theorized only to be present in the beginning of a surface contact while it is negligible for prolonged or repeated contacts [20]. That is, when machine parts slide against each other for millions of cycles, the plastic deformation would only take place in the beginning for which the system then reaches a steady state with only elastic deformations. The chemical friction arises from adhesion between microscopic contacting surfaces, with an energy loss attributed to the breaking and forming of bonds.

2.3.1 Asperity theories

Asperity theories have their foundations in the adhesion model proposed by Bowden and Tabor [21] which is based on the fundamental reasoning that friction is governed by the adhesion between two surfaces [22]. Adhesion is proportional to the real contact area defined by asperity junctions and interfacial shear strength τ between such contacting junctions. For an asperity contact area A_{asp} we get a true contact area $\sum A_{\text{asp}}$ leading to

$$F_{\text{fric}} = \tau \sum A_{\text{asp}}.$$

²You would most likely have a good shot at the Nobel Prize with that paper.

Note that this is still compatible with Amontons' law in Eq. (2.1) by having a linear relationship between the real contact area and the applied load. In fact, this is exactly how the theoretical model explains the friction dependency of load. By increasing the normal load it is hypothesized that the real contact area will increase as the asperity tips are deformed (plastically or elastically) into broader contact points as visualized qualitatively in Fig. 2.2.

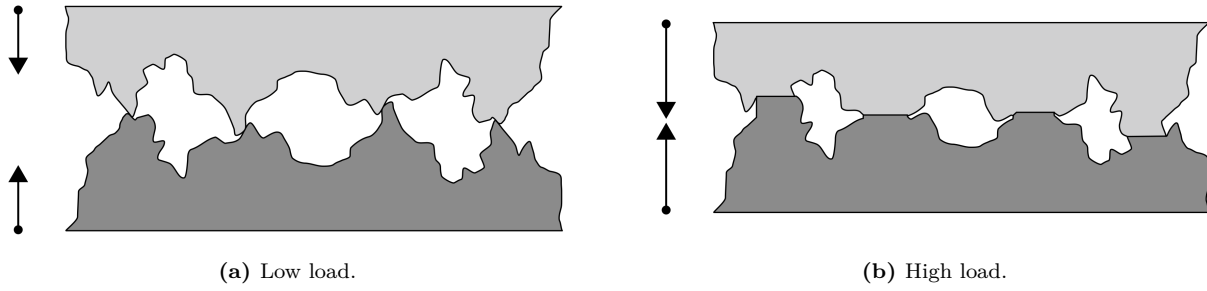


Figure 2.2: Qualitative illustration of the microscopic asperity deformation under increasing load from frame (a) to (b) [23]. While this figure seemingly portrays plastic deformation the concept of increased contact area under increased load applies for elastic deformation as well.

Many studies have focused on single asperity contacts to reveal the relationship between the contact area and load [24–26]. By assuming perfectly smooth asperities, with radii of curvature from micrometers all the way down to nanometers, continuum mechanics can be used to predict the deformation of asperities as load is applied. A model for non-adhesive contact between homogenous, isotropic, linear elastic spheres was first developed by Hertz [27], which predicted $A_{\text{asp}} \propto F_N^{2/3}$. Later adhesion effects were included in a number of subsequent models, including Maugis-Dugdale theory [28], which also predicts a sublinear relationship between A_{asp} and F_N . Thus, the common feature of all single-asperity theories is that A_{asp} is a sublinear function of F_N , leading to a similar sublinear relationship for $F_{\text{fric}}(F_N)$, which fails to align with the macroscale observations modelled by Amontons' law (eq. (2.1)).

Concurrently with single-asperity studies, roughness contact theories are being developed [29–32] to bridge the gap between single asperities and macroscopic contacts [19]. A variety of multi-asperity theories has attempted to combine single asperity mechanics by statistical modelling of the asperity height and spatial distributions [20]. This has led to a partially success in the establishment of a linear relationship between A_{asp} and F_N . Unfortunately, these results are restricted in terms of the magnitude of the load and contact area, where multi-asperity contact models based on the original ideas of Greenwood and Williamson [31] only predicts linearity at vanishing low loads, or Persson [30] which predicts linearity for more reasonable loads but only up to 10-15 % of the macroscale contact area. However, as the load is further increased all multi-asperity models predict the contact area to fall into the sublinear dependency of normal force as seen for single asperity theories as well [20].

2.4 Nanoscale — Atomic scale

Going from a micro- to a nanoscale, on the order of 10^{-9} m, it has been predicted that continuum mechanics will start to break down [33] due to the discreteness of individual atoms. In a numerical MD study by Mo et al. [19], considering asperity radii of 5-30 nm, it has been shown that the asperity area A_{asp} , defined by the circumference of the contact zone, is sublinear with F_N . This is accommodated by the observation that not all atoms within the circumference make chemical contact with the substrate. By modelling the real contact area $A_{\text{real}} = N A_{\text{atom}}$, where N is the amount of atoms within the range of chemical interaction and A_{atom} the associated surface area for a contacting atom, they found a consistent linear relationship between friction and the real contact area. Without adhesive forces this lead to a similar linear relationship $F_{\text{fric}} \propto F_N$, while adding van der Waals adhesion to the simulation gave a sublinear relationship matching microscale single asperity theory, even though the $F_{\text{fric}} \propto A_{\text{real}}$ was maintained. This result emphasizes that the predictions of continuum mechanics might still apply at the nanoscale and that the contact area can still be expected to play an

important role for nanoscale asperity contact. It is simply the definition of the contact area that undergoes a change when transitioning from micro- to nanoscale.

While the study by Mo et al. [19] considers a single asperity on a nanoscale, some models take this even further to what we will denote as the atomic-scale. This final leap is motivated by the fact that our system of interest, an atomically flat graphene sheet imposed on a flat silicon substrate, lacks the presence of nanoscale asperities in its initial uncut undeformed state. In the lack of noteworthy structural asperities, friction can instead be modelled as a consequence of the “rough” potential laid out by the atomic landscape. A series of so-called reduced-order models builds on a simplified system of atomic-scale contacts based on three essential parts: 1) A periodic potential modelling the substrate as rigid crystalline surface. 2) An interacting particle, or collection of particles, placed in the potential. 3) A moving body, moving at steady speed, and connected to the particles through a harmonic coupling. In figure Fig. 2.3 three of the most common 1D models is displayed which we will address in the following sections. The time-honored Prandtl-Tomlinson (PT) model describes a point-like tip sliding over a space-periodic fixed crystalline surface with a harmonic coupling to the moving body. This is analog to that of an experimental cantilever used for Atomic Force Microscopy which we will introduce in more details in Sec. 2.4.5.1. Further extensions was added in the Frenkel-Kontorova (FK) model by substituting the tip with a chain of harmonic coupled particles dragged from the end, and finally combined in the Frenkel-Kontorova-Tomlinson (FKT) with the addition of a more rigorous harmonic coupling between the moving body and each of the atoms in the chain. While these models cannot provide the same level of details as atomistic simulations such as MD it enables investigation of atomic friction under most conditions, some of which are inaccessible to MD [34]. This makes these models an appropriate tool for investigating individual parameters and mechanisms governing affecting friction.

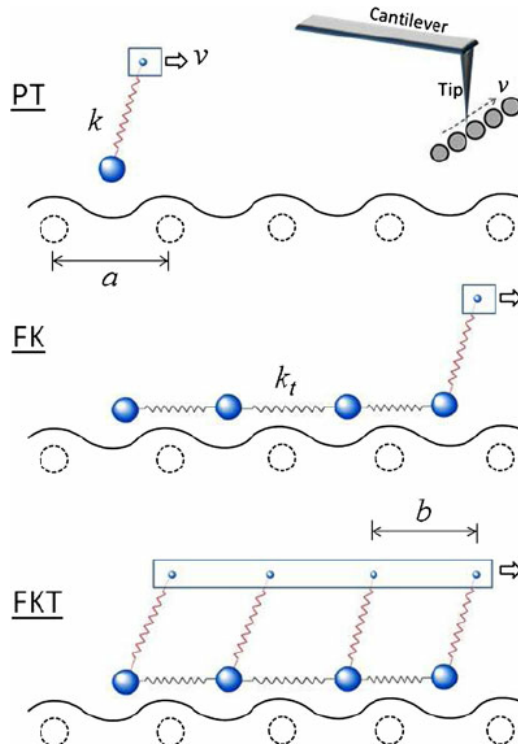


Figure 2.3: Temporary figure from [34]. Be careful to align notation on the figures with the text later on.

2.4.1 Prandtl–Tomlinson

We consider the Prandtl–Tomlinson model (PT) with added thermal activation as proposed by Gnecco et al. [35]. For the theoretical foundation of this section we generally refer to [34].

The 1D PT model assumes a single ball-tip coupled harmonically to a support moving at constant speed which makes the tip slide along the rigid substrate. The interaction between tip and substrate is modelled as a sinusoidal corrugation potential mimicking the periodicity found in a crystalline substrate. The total potential

energy is given as

$$V(x, t) = \frac{1}{2}K(vt - x)^2 - \frac{1}{2}U_0 \cos\left(\frac{2\pi x}{a}\right). \quad (2.3)$$

The first term describes the harmonic coupling at time t , with spring constant K , between the tip at position x and the moving body at position vt , given by its constant speed v . The second term describes the corrugation potential with amplitude U_0 and period a representing the lattice spacing of the substrate. The dynamics of the tip can be described by the Langevin equations

$$m\ddot{x} + m\mu\dot{x} = -\frac{\partial V(x, t)}{\partial x} + \xi(t), \quad (2.4)$$

Match notation with later use.

where m is the mass of the tip, μ the viscous friction and $\xi(t)$ the thermal activation term. The equation is solved for tip position x and the friction force is retrieved as the force acting on the moving body

$$F_{\text{fric}} = K(vt - x).$$

The governing equation Eq. (2.4) belongs to a family of stochastic differential equations composed of deterministic dynamics and stochastic processes. In this case the deterministic term is the viscous friction, $m\mu\dot{x}$, to resist the movement of the tip and the force acting from the corrugation potential. The stochastic term is a random force field modelling thermal noise according to the fluctuation–dissipation relation. Thus, there is no single path but rather multiple paths the tip can take. While the Langevin equations is one of the most common ways to handle thermal activaiton other methods exist to solve this problem such as Monte Carlo sampling methods. We omit the numerical scheme for solving this and refer to a more in depth discussion of the Langevin equations with respect to the use in MD simulations in Sec. 3.3.1.

2.4.1.1 Thermal activation

The solving of the Langevin equations, as opposed to Newtons equation of motion, introduces thermal effects to the system. Generally, when the energy barrier comes close to $k_B T$ (0.026 eV at room temperature) thermal effects can not be neglected. In the case of a single asperity contact the energy barrier is on the order 1 eV which make thermal activation significant [34]. Due to the moving body travelling at constant speed the potential energy will increase steadily. Without any temperature, $T = 0$, the slip will only accour when the energy barrier between the current potential well (i) and the adjacent (j) is zero $\Delta V_{i \rightarrow j} = 0$. However, in the presence of temperature we get thermal activation, meaning that the tip can slip to the next potential well sooner $\Delta V_{i \rightarrow j} > 0$. Provided that the sliding speed is slow enough (**Elaborate**) the transistion rate κ for a slip from the current to the next well is given by

$$\kappa = f_0 e^{-\Delta V/k_B T}, \quad (2.5)$$

with ΔV being the energy barrier and f_0 the attempt rate. The attempt rate following Kramer's rate theory [36] is related to the mass and damping of the system and can be thought of as the frequency which the tip “attempts” to overcome the barrier. Notice that Eq. (2.5) resembles a microstate probability in the canonical ensemble with f_0 in place of the inverse partion function Z^{-1} which can be used as another intepretation of f_0 . The probability p_i that the tip occupies the current well i relative to the adjacent well j , as illustrated in Fig. 2.4 is governed by

$$\frac{dp_i}{dt} = -\kappa_{i \rightarrow j} p_i + \kappa_{j \rightarrow i} p_j.$$

This probability is related to temperature, speed and mass.

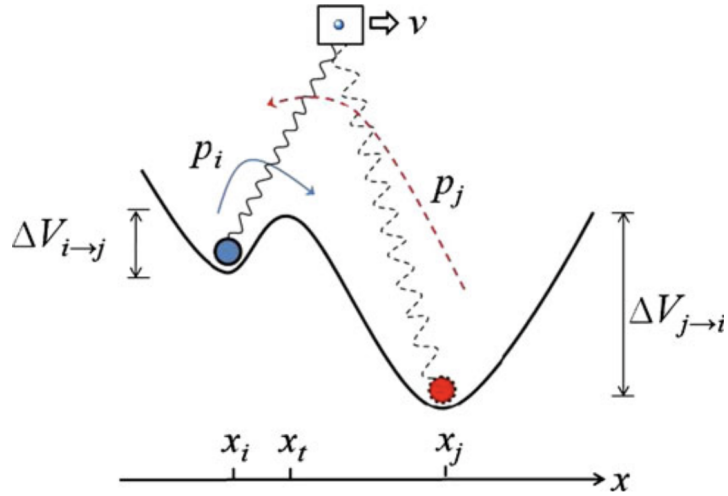


Fig. 3 An illustration of slip between two adjacent energy minima. p_i is the probability of the tip residing in the current potential well, i , where the energy barrier is $\Delta V_{i \rightarrow j}$. p_j is the probability of the tip residing at the next minima, j , where $\Delta V_{j \rightarrow i}$ is the corresponding energy barrier

Figure 2.4: [Temporary] figure from [34]

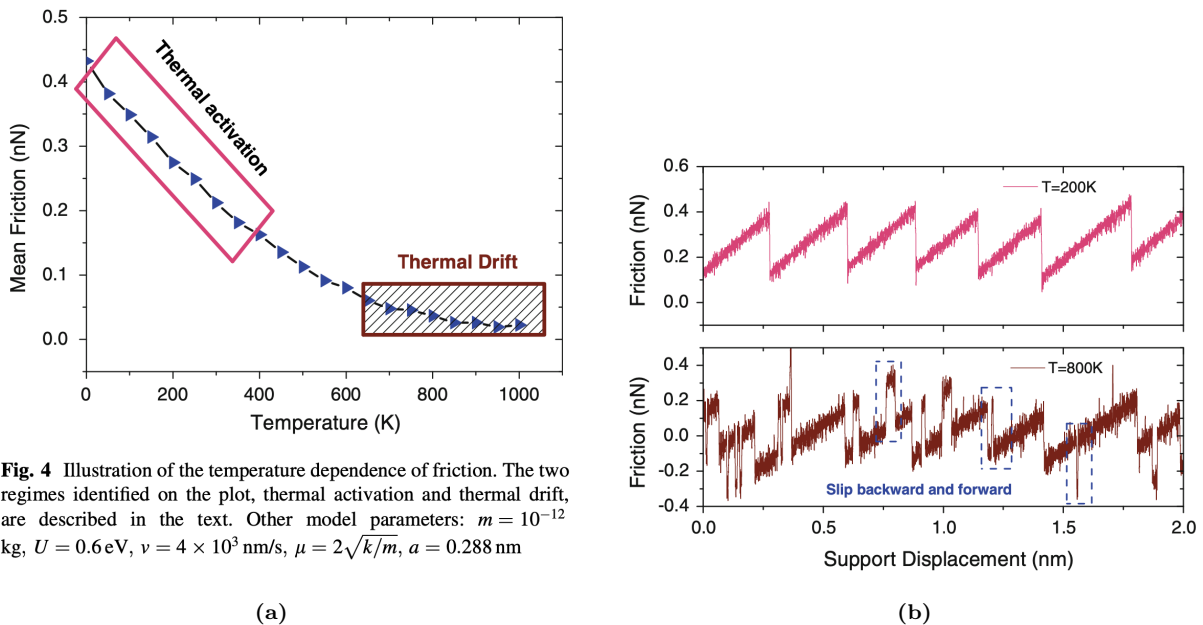


Fig. 4 Illustration of the temperature dependence of friction. The two regimes identified on the plot, thermal activation and thermal drift, are described in the text. Other model parameters: $m = 10^{-12}$ kg, $U = 0.6$ eV, $v = 4 \times 10^3$ nm/s, $\mu = 2\sqrt{k/m}$, $a = 0.288$ nm

Figure 2.5: [Temporary] figures from [34]

Generally, there exist two temperature regimes in the model: Thermal activation at low temperature and thermal drift at high temperature as shown in Fig. 2.5. At lower temperature the system is subject to standard thermal activation with $\Delta V_{i \rightarrow j} \gg \Delta V_{j \rightarrow i}$ resulting in $\kappa V_{i \rightarrow j} \gg \kappa V_{j \rightarrow i}$. Effectively, this inhibits any backwards

slip and we get

$$\frac{dp_i}{dt} = -\kappa_{i \rightarrow j} p_i,$$

which make the relationship between friction, temperature and speed follow Sang et al.'s prediction [37]

$$F = F_c - \left| \beta k_B T \ln \left(\frac{v_c}{v} \right) \right|^{2/3}, \quad v_c = \frac{2f_0 \beta k_B T}{3C_{\text{eff}} \sqrt{F_c}}, \quad (2.6)$$

where F_c is the maximum friction at $T = 0$, v_c a critical velocity, f_0 is the attempt rate, C_{eff} the effective stiffness, and β a parameter determined by the shape of the corrugation well. Eq. (2.6) characterizes the decrease in friction with temperature in the thermal activation regime, shown in Fig. 2.5a at low temperature, with the assumption of only forward slips, as seen in the force trace shown in Fig. 2.5a. When the temperature is high enough, for the system to be consistently close to thermal equilibrium, it enters the regime of thermal drift [38]. This regime transition can be understood through a comparison of two time scales: The time it takes for the moving body to travel one lattice spacing $t_v = a/v$ and the average time for a slip to occur due to thermal activation $\tau = 1/\kappa = f^{-1} \exp(\Delta V/k_B T)$. If $t_v \gg \tau$ the system falls within the thermal drift regime, with slips both backwards and forwards as shown in Fig. 2.5b, and the friction follows the prediction of Krylov et al. [38–40]

$$F \propto \frac{v}{T} e^{1/T}.?? \quad (2.7)$$

2.4.1.2 Sliding speed

In the thermal activation regime (low temperature) and at low speeds the friction relation follows Eq. (2.6) making friction scale logarithmically with speed. For higher speed, $v > v_c$, if only thermal effects are considered, Eq. (2.6) predicts that friction will eventually saturate and come to a plateau at $F_{\text{fric}} = F_c$. This is illustrated in Fig. 2.6 with this prediction being represented by the dotted line. However, as given away by the figure, for higher speed the model will enter an athermal regime where the thermal effects are negligible compared to other contributions [34](32). In the athermal regime the damping term $m\mu\dot{x}$ will dominate yielding $F_{\text{fric}} \propto v$. The athermal regime is often observed in reduced models if the system is overdamped or at high speeds. This concept is also interesting in connection to MD simulations where the accessible speeds often fall into the athermal regime [41]. It is unclear how this affects real physical systems for which there exist more dissipation channels than just a single viscous term [42]. For the thermal drift regime at higher temperatures the linear relation $F_{\text{fric}} \propto v$ is predicted for low speed as well by ??.

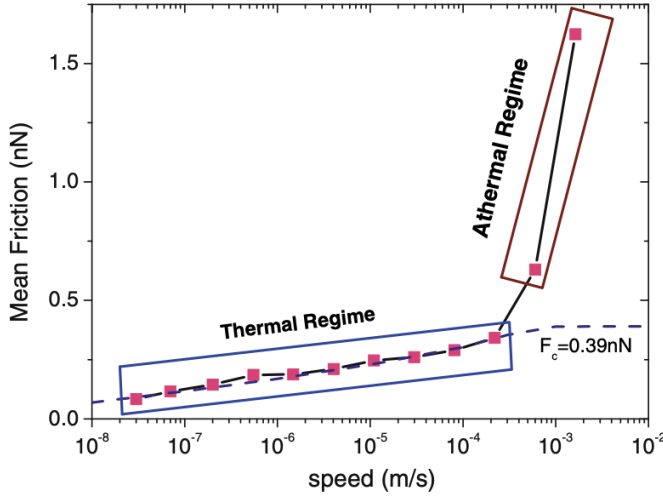


Fig. 6 Speed dependence of friction illustrating two different regimes. In the thermal regime, there is a logarithmic scaling of friction with speed, and in the athermal regime the friction is governed by the damping term such that $F \propto v$. The friction plateau ($F_c = 0.39$ nN) predicted by thermal activation is identified by the dashed line. Other model parameters: $m = 10^{-12}$ kg, $U = 0.6$ eV, $T = 300$ K, $v = 4 \times 10^3$ nm/s, $\mu = 2\sqrt{k/m}$, $a = 0.288$ nm

Figure 2.6: Temporary figure from [34]

2.4.1.3 Tip mass

The mass of the tip affects the dynamics due to a change of inertia, which changes the attempt rate f_0 . A smaller inertia leads to a larger attempt rate and vice versa. Effectively, this will affect the transition point for the temperature and speed regimes described in the previous. A smaller inertia, giving a larger attempt rate, will cause an earlier transition (i.e. at lower temperature) to the thermal drift regime, and result in a later speed saturation such that it transitions to the athermal regime at higher speed.

2.4.1.4 Friction Regimes: Smooth Sliding, Single Slip, and Multiple Slip

Stick-slip motion is a crucial instability mechanism associated with high energy dissipation and high friction. Thus, controlling the transition between smooth sliding and stick-slip is considered key to control friction. We can divide the frictional stick-slip behaviour into three regimes: 1) Smooth sliding, where the tip slides smoothly on the substrate. 2) Single slip, where the tip sticks at one potential well before jumping one lattice spacing to the next. 3) Multiple slip, where the tip jumps more than one lattice spacing for a slip event. The underlying mechanisms behind these regimes can be understood through a static and a dynamic contribution.

To understand the static mechanism we consider a quasistatic process for which temperature, speed and damping can be neglected and where we must have $\partial(V)/\partial x = 0$. This simplifies Eq. (2.3) to

$$\frac{\pi U_0}{a} \sin\left(\frac{2\pi x}{a}\right) \frac{2\pi}{a} = K(vt - x). \quad (2.8)$$

The friction regime is determined by the number of solutions x to Eq. (2.8). Only one solution corresponds to smooth sliding, two solutions to a single slip and so on. It turns out that the regimes can be defined by the parameter $\eta = 2\pi^2 U_0/a^2 K$ [43, 44] yielding transitions at $\eta = 1, 4.6, 7.79, 10.95, \dots$, such that $\eta \leq 1$ corresponds to smooth sliding, $1 < \eta \leq 4.6$ to a single slip and so on. These static derivation lays out the fundamental probabilities for being in one of the regimes stick-slip regimes.

Considering the dynamics on top, one finds that damping, speed and temperature will affect this probability. A high damping, equivalent of a high transfer of kinetic energy to heat, will result in less energy available for

the slip events. This will make multiple slip less likely. By a similar argument, we find that increasing the speed will contribute to more kinetic energy which will increase the likelihood of multiple slips. Finally, temperature will contribute to earlier slips, due to thermal activation, such that less potential energy can be accumulated and it will result in fewer multiple slips. The effects of damping, speed and temperature is illustrated for the force traces in Fig. 2.7

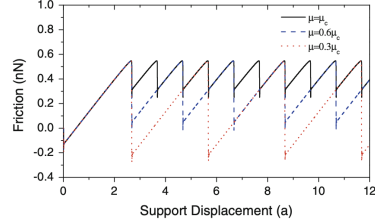


Fig. 9 The effect of damping on transitions between slip regimes where $\mu_c = 2\sqrt{k/m}$ is the critical damping coefficient. Single, double, and triple slip occur at $\mu = \mu_c$, $0.6 \mu_c$, and $0.3 \mu_c$, respectively. The abscissa has units of the lattice spacing a to facilitate identification of the transitions between single, double, and triple regimes. Other model parameters: $U = 0.6 \text{ eV}$, $T = 0 \text{ K}$, $v = 1 \mu\text{m/s}$, $m = 10^{-12} \text{ kg}$, $k = 1 \text{ N/m}$, $a = 0.288 \text{ nm}$

(a)

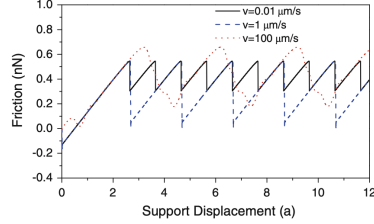


Fig. 10 The effect of sliding speed on transitions between slip regimes. Single, double, and triple slip occur at $v = 100$, 1 , and $0.01 \mu\text{m/s}$, respectively. Other model parameters: $U = 0.6 \text{ eV}$, $T = 0 \text{ K}$, $\mu = 0.8 \mu_c$, $m = 10^{-12} \text{ kg}$, $k = 1 \text{ N/m}$, $a = 0.288 \text{ nm}$

(b)

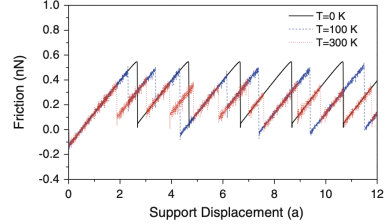


Fig. 11 The effect of temperature on transitions between slip regimes. Other model parameters: $U = 0.6 \text{ eV}$, $v = 1 \mu\text{m/s}$, $\mu = 0.6 \mu_c$, $m = 10^{-12} \text{ kg}$, $k = 1 \text{ N/m}$, $a = 0.288 \text{ nm}$

(c)

Figure 2.7: Temporary figure from [34]

2.4.2 Frenkel-Kontorova

The Frenkel-Kontorova (FK) model [45] extends the PT model by considering a chain of atoms in constraint to just a single particle (tip). This extension is useful for understanding the importance of the alignment between the atoms and the substrate, the so-called *commensurability*.

The standard (FK) model consists of a 1D chain of N classical particles of equal mass, representing atoms, interacting via harmonic forces and moving in a sinusoidal potential as sketched in Fig. 2.8 [15]. The hamiltonian is

$$H = \sum_{i=1}^N \left[\frac{p_i^2}{2m} + \frac{1}{2} K(x_{i+1} - x_i - a_c)^2 + \frac{1}{2} U_0 \cos\left(\frac{2\pi x_i}{a_b}\right) \right], \quad (2.9)$$

where the atoms are labelled sequentially $i = 1, \dots, N$. The first term $p_i^2/2m$ represents the kinetic energy with momentum p_i and mass m . Often the effects of inertia are neglected, referred to as the static FK model, while the inclusion in Eq. (2.9) is known as the dynamic FK model [46]. The next term describes the harmonic interaction with elastic constant K , nearest neighbour distance $\Delta x = x_{i+1} - x_i$ and corresponding nearest neighbour equilibrium distance a_c . The final term represents the periodic corrugation potential, with amplitude U_0 and period a_b . By comparison to the potential used in the PT model Eq. (2.3), the only difference is the introduction of a harmonic coupling between particles in the chain as opposed to the moving body, and that we have not yet specified any force incentivizing sliding. Different boundary choices can be made where both free ends and periodic conditions give similar results. The choice of fixed ends however makes the chain incapable of sliding.

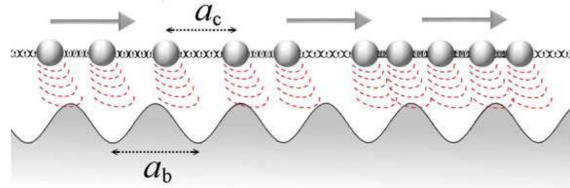


Figure 1. A sketch of the FK model, showing the two competing lengths: the average interparticle spacing and the lattice periodicity of the substrate.

Figure 2.8: [Temporary figure from [15]]

To probe static friction one can apply an external adiabatically increasing force until sliding accours. This corresponds to the static FK model, and it turns out that the sliding properties are entirely governed by its topological excitations referred to as so-called *kinks* and *antikinks*

2.4.2.1 Commensurability

We can subdivide the frictional behaviour in terms of commensurability, that is, how well the spacing of the atoms match the periodic substrate potential. We describe this by the length ratio $\theta = a_b/a_c = N/M$ where M denotes the number of minemas in the potential (within the length of the chain). A rational number for θ means that we can achieve a perfect alignment between the atoms in the chain and the potential minemas, without stretching the chain, corresponding to a *commensurate* case. If θ is irrational the chain and substrate cannot fully align without some stretching of the chain, and we denote this as being *incommensurate*.

We begin with the simplest commensurate case of $\theta = 1$ where the spacing of the atoms matches perfectly with the substrate potential periodicity, i.e. $a_c = a_b$, $N = M$. The ground state (GS) is the configuration where each atom is aligned with one of the substrate minema. By adding an extra atom to the chain we would effectively shift over some of the atoms, out of this ideal state, giving rise to a kink excitation. This leads to the case where two atoms will have to “share” the same potential corrugation as sketched in Fig. 2.10. On the other hand, removing an atom from the chain results in an antikink excitation where one potential corrugation will be left “atomless”. In order to reach a local minimum the kink (antikink) will expand in space over a finite length such that the chain undertakes a local compression (expansion). Notice that for low ratios of θ , fewer atoms than minema, the chain will not be able to fill each corrugation well in any case, meaning that commensurability can instead be thought of as whether the atoms are forced to deviate, by a lattice spacing, from the spacing otherwise dictated by the spring forces inbetween. When applying a tangential force to the chain it is much easier for an excitation to move along the chain than it is for the non-excited atoms since the activation energy ϵ_{PN} for a kink/antikink displacement is systematically smaller (often much smaller) than the potential barrier U_0 . Thus, the motion of kinks (antikinks), i.e. the displacement of extra atoms (atom vacancies), is represententing the fundamental mechanism for mass transport. These displacements are responsible for the mobility, diffusivity and conductivity within this model.

In the zero temperature commensurable case with an adiabatical increase in force, all atoms would be put into an accelerating motion as soon as the potential barrier energy is present. However, just as discussed for the PT model, thermal activations will excite the system at an earlier stage resulting in kink-antikink pairs traveling down the chain. For a chain of finite length these often accrour at the end of the chain running in opposite direction. This cascade of kink-antikink exications is shown in Fig. 2.9. Notice, that for the 2D case, where an island (or flake) is deposited on a surface, we generally also expect the sliding to be initiated by kink-antikink pairs at the boundaries.

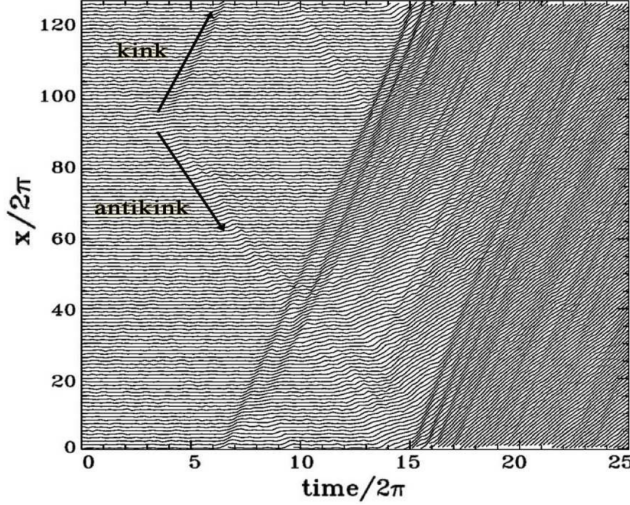


Figure 2. Time dependence of the atomic trajectories for the fully matched ($\theta = 1$) FK model at the (low-temperature) onset of depinning. Motion starts with the nucleation of a kink-antikink pair. The kink and the antikink depart in opposite directions cross the periodic boundary conditions, and collide quasielastically. A second kink-antikink pair forms in the wake of the initial kink. Further kink-antikink pairs are generated, with an avalanche-like increase of the kink-antikink concentration, eventually leading to a sliding state. Adapted from Ref. [21], Copyright (1997) by The American Physical Society.

Figure 2.9: [Temporary] figure from [15]

For the case of incommensurability, i.e. $\theta = a_b/a_c$ is irrational, the GS is characterized by a sort of “staircase” deformation. That is, the chain will exhibit regular periods of regions where the chain is slightly compressed (expanded) to match the substrate potential, separated by kinks (antikinks), where the increased stress is eventually released.



Figure 2.10: [Temporary] figure from [urlhttp://www.iop.kiev.ua/~obraun/myreprints/surveyfk.pdf](http://www.iop.kiev.ua/~obraun/myreprints/surveyfk.pdf) p. 14. Incommensurable case ($\theta = ?$) where atoms sit slightly closer than otherwise dictated by the substrate potential for which this regularly result in a kink here seen as the presence of two atoms closely together in one of the potential corrugations.

The incommensurable FK model contains a critical elastic constant K_c , such that for $K > K_c$ the static friction F_s drops to zero, making the chain able to initiate a slide at no energy cost, while the low-velocity kinetic friction is dramatically reduced. This can be explained by the fact that the displacement occurring in the incommensurable case will yield just as many atoms climbing up a corrugation as there are atoms climbing down. For a big (infinite) chain this will exactly balance the forces making it non-resistant to sliding. Generally, incommensurability guarantees that the total energy (at $T = 0$) is independent of the relative position to the potential. However, when sliding freely, a single atom will eventually occupy a maximum of the potential, and thus when increasing the potential magnitude U_0 or softening the chain stiffness, lowering K , the possibility to occupy such a maximum disappears. This marks the so-called Aubry transition, at the critical elastic constant $K = K_c(U_0, \theta)$, where the chain goes from a free sliding to a pinned state with a nonzero static friction. K_c is a discontinuous function of the ratio θ , due to the reliance on irrational numbers for incommensurability. The minimal value $K_c \simeq 1.0291926$ in units $[2U_0(\pi/a_b)^2]$ is achieved for the golden-mean ratio $\theta = (1 + \sqrt{5})/2$.

Notice that the pinning is provided despite translational invariance due to the inaccessibility to move past the energy barrier which act as a dynamical constraint. The Aubry transition can be investigated as a first-order phase transition for which power laws can be defined for the order parameter, but this is beyond the scope of this thesis.

The phenomena of non-pinned configurations is named *superlubricity* in tribological context. Despite the misleading name this refers to the case where the static friction is zero while the kinetic friction is nonzero but reduced. For the case of a 2D sheet it is possible to alter the commensurability, not only by changing the lattice spacing through material choices, but also by changing the orientation of the sheet relative to the substrate. Dienwiebel et al. [47] have shown that the kinetic friction, for a graphene flake sliding over a graphite surface (multiple layers of graphene), exhibits extremely low friction at certain orientations as shown in Fig. 2.11. Here we clearly see that friction changes as a function of orientation angles with only two spikes of considerable friction force. This relates back to the concept of frictional regimes introduced through the simpler PT model, where the change in orientation affects the effective substrate potential. Merely from the static consideration, we found that lowering the potential amplitude U_0 will decrease the parameter $\eta = 2\pi^2 U_0/a^2 K$ shifting away from the regime of multiple slips towards smooth sliding associated with low friction. Such transitions will also be affected by the shape of the potential and corresponding 2D effects of the sliding path [34].

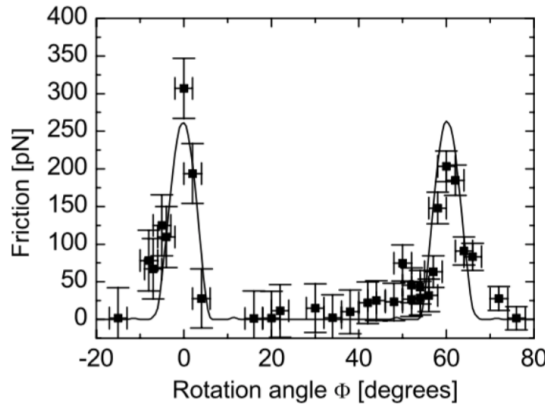


Fig. 6. Average friction force versus rotation angle Φ of the graphite sample around an axis normal to the sample surface. Two narrow peaks of high friction are observed at 0° and 61° , respectively. Between these peaks a wide angular range with ultra-low friction, close the detection limit of the instrument, is found. The first peak has a maximum friction force of 306 ± 40 pN, and the second peak has a maximum of 203 ± 20 pN. The curve through the data points shows results from a Tomlinson model for a symmetric 96-atom graphite flake sliding over the graphite surface (for details about the calculation see [39]).

Figure 2.11: [Temporary] figure from [47] showing superlubricity for incommensurable orientations between graphene and graphite. [temporary]

2.4.2.2 Velocity resonance

While many of the same arguments used for the PT model regarding velocity dependence for friction can be made for the FK model, the addition of multiple atoms introduces the possibility of resonance. In the FK model the kinetic friction is primarily attributed to resonance between the sliding induced vibrations and phonon modes in the chain [46]. The specific dynamics is found to be highly model and dimension specific, and even for the 1D case this is rather complex. However, we make a simplified analysis of the 1D rigid chain case to showcase the reasoning behind the phenomena.

When all atoms are sliding rigidly with center of mass velocity v_{CM} the atoms will pass the potential maxima with the so-called *washboard frequency* $\Omega = 2\pi v_{CM}/ab$. For a weak coupling between the chain and the potential we can use the zero potential case as an approximation for which the known dispersion relation for the 1D

harmonic chain is given [48, p. 92]

$$\omega_k = \sqrt{\frac{4K}{m}} \left| \sin\left(\frac{k}{2}\right) \right|,$$

where ω_k is the phonon frequency and $k = 2\pi i/N$ the wavenumber with $i \in [N/2, N/2)$. Resonance will occur when the washboard frequency Ω is close to the frequency of the phonon modes ω_q in the chain with wavenumber $q = 2\pi a_c/a_b = 2\pi\theta^{-1}$ or its harmonics nq for $n = 1, 2, 3, \dots$ [49]. Thus, we can approximate the resonance center of mass speed as

$$\begin{aligned} n\Omega &\sim \omega_{nq} \\ n\frac{2\pi v_{CM}}{a_b} &\sim \sqrt{\frac{4K}{m}} \left| \sin\left(\frac{2n\pi\theta^{-1}}{2}\right) \right| \\ v_{CM} &\sim \frac{\sin(n\pi\theta^{-1})}{n\pi} \sqrt{\frac{Ka_b^2}{m}}. \end{aligned}$$

When the chain slides with a velocity around resonance speed, the washboard frequency can excite acoustic phonons which will dissipate to other phonon modes as well. At zero temperature, the energy will transform back and forth between internal degrees of freedom and center of mass movement of the chain. Without any dissipation mechanism this is actually theorized to speed up the translational decay [46]. However, as soon as we add a dissipation channel through the substrate, energy will dissipate from the chain to the substrate degrees of freedom. This suggests that certain sliding speeds will exhibit relatively high kinetic friction while others will be subject to relative low kinetic friction. Simulations of concentric nanotubes in relative motion (telescopic sliding) supports this idea as it has revealed the occurrence of certain velocities at which the friction is enhanced, corresponding to the washboard frequency of the system [15], where the friction response was observed to be highly non-linear as the resonance velocities were approached.

The analysis of the phonon dynamics is highly simplified here, and a numerical study of the FK by Norell et al. [46] showed that the behaviour was highly dependent on model parameter choices, but that the friction generally increased with velocity and temperature. Here the latter observation differs qualitative from that of the PT model.

2.4.3 Frenkel-Kontorova-Tomlinson

A final extension of the atomic models worth mentioning here is the Frenkel-Kontorova-Tomlinson (FKT) model [50], which introduces a harmonic coupling of the sliding atom chain to the driving moving body, effectively combining PT and FK (see Fig. 2.3). This introduces more degrees of freedom to the model based on the intention of getting a more realistic connection between the moving body and the chain. modelling of a broad contact point. Dong et al. carried out a numerical analysis using the 1D FKT model investigating the effect of chain length. They observed that the friction increased linearly with number of atoms in the chain on a long range, but certain lattice mismatch resulted in local non-linear relationship as shown in Sec. 2.4.3. Similar, taking the FKT model to 2D they were able to achieve a similar sensitivity to commensurability as observed experimentally by [47] (shown in Fig. 2.11) with the numerical result shown in Sec. 2.4.3. Besides a recreation of the commensurability effect they also observed increasing friction with an increasing flake size. Combined, the 1D and 2D results supports the idea of an increasing friction with contact size although it might showcase non-linear behaviour depending on commensurability.

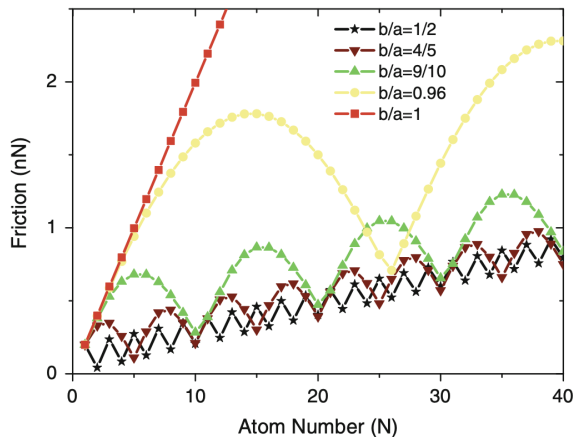


Fig. 21 Friction variation with the tip size N for different lattice mismatch b/a . $k = 5 \text{ N/m}$ and $k_t = 50 \text{ N/m}$ are used to obtain these results

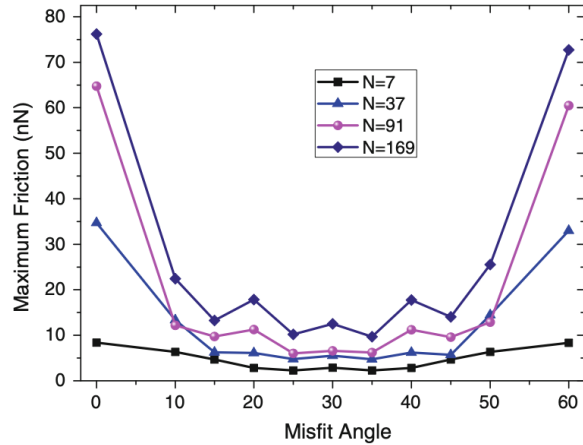


Fig. 23 The misfit angle dependence of friction with different tip sizes; $k_t = 50 \text{ N/m}$ and $k = 10 \text{ N/m}$. The $N = 7$ curve corresponds to the model illustrated in Fig. 22

(a) [Temporary] figure from [34]

(b) [Temporary] figure from [34]

2.4.4 Shortcomings of atomic models

To-DO: Shortcomings of PT-based reduced-models

- Assumes a rigid substrate with a simplified potential shape.
- Energy dissipation is added through a viscous term $-m\mu\dot{x}$ being the only dissipation channel available. Does not capture a more complex real life electron and phonon dissipation. Taking phonon dissipation as an example there are many vibrational modes ($3N$). This will effect the thermal activation derivation.
- The moving body is simplified as constant moving rigid body, while in fact this will also be subject to a more complex dynamic behavior.

2.4.5 Experimental procedures

Experimentally, the study of nanoscale friction is challenging due to the low forces on the scale of nano-newtons along with difficulties of mapping the nano-scale topography of the sample. In opposition to numerical simulations, which provides full transparency regarding atomic-scale structures, sampling of forces, velocities and temperature, the experimental results are limited by the state-of-the-art experimental methods. In order to compare numerical and experimental results it is useful to address the most common experimental.

2.4.5.1 Scanning Probe Microscopy

Scanning probe microscopy (SPM) includes a variety of experimental methods which is used to examine surfaces with atomic resolution [51, pp. 6-27]. This was originally developed for surface topography imaging, but today it plays a crucial role in nanoscale science as it is used for probe-sampling regarding tribological, electronic, magnetic, biological and chemical character. The family of methods involving the measurement of forces is generally referred to as *scanning force microscopies* (SFM) or for friction purposes *friction force microscopes* (FFM).

One such method arose from the *atomic force microscope* AFM, which consists of a sharp micro-fabricated tip attached to a cantilever force sensor, usually with a sensitivity below 1 nN all the way down to pN. The force is measured by recording the bending of the cantilever, either as a change in electrical conduction or more commonly, by a light beam reflected from the back of the cantilever into a photodetector [1, p. 183]. By adjusting the tip-sample height to keep a constant normal force while scanning across the surface this can be used to produce a surface topography map. By tapping the material (dynamic force microscopy) with sinusoidally

vibrated tip the effects from friction and other disturbing forces can be minimized in order to produce an even clearer image (include example, preferable showing the surface structure of graphene). However, when scanning perpendicularly to the cantilever axis, one is also able to measure the frictional force as torsion of the cantilever. By having four quadrants in the photodetector (as shown in figure Fig. 2.13), one can simultaneously measure the normal force and friction force as the probes scans accross the surface.

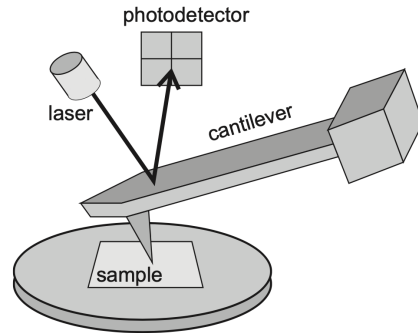


Figure 17.1 Schematic diagram of a beam-deflection atomic force microscope.

Figure 2.13: [Temporary figure from [1, p. 184]

AFM can also be used to drag a nanoflake accross the substrate as done by Dienwiebel et al. [47], where a graphene flake was attached to a FFM tip and dragged accross graphite. Notice that this makes the normal loading concentrated to a single point on the flake rather than achieving an evenly distributed load.

2.4.5.2 Surface Force Apparatus

The Surface force apparatus SFA is based on two curved molecularly smooth surfaces brought into contact [1, p. 188]. The sample is placed in between the two surfaces as surfaces as lubricant film for which the friction properties can be studied by applying a tangential force to the surfaces.

2.5 Expected frictional properties of graphene

Several studies have investigated the frictional behaviour of graphene by varying different parameters such as normal force, sliding velocity, temperature, commensurability and graphene thickness [52]. In general, we find three types of relevant systems being studied: 1) An FFM type setup where the graphene, either resting on a substrate or suspended, is probed by an AFM tip scanning across the surface. 2) SFA approach with the graphene “sandwiched” in between two substrate layers moving relative to each other using the graphene as a solid lubricant. 3) A graphene flake sliding on a substrate, either being dragged by an AFM tip or by more complex arrangements in numerical simulations. Considering that even the sharpest AFM tip will effectively put multiple atoms in contact with the test sample, all methods relates to a nanoscale contact involving graphene but differs on contact area. However, the FFM type suggest a basis in asperity theory as we expect it to deform with increasing load, while the latter two is more aligned with the PT type models and our system our interest which is an atomic flat sheet on a flat substrate. Having said that, we consider all three types with the purpose of gaining a more comprehensive insight. The relevant studies considered in the following are listed in Table 2.1 for convenience.

Table 2.1: Update multirow line span after completing the table...

System	Type	Year	Researcher	Materials	Key words
FFM	Exp.	2007 [53]	Zhao et al.	Si ₃ N ₄ tip on graphite.	Temperature dependence
		2015 [54]	G. Paolicelli et al.	Si tip, graphene on SiO ₂ and Ni(111) substrate	Layers, load, shear strength
	Mix	2019 [55]	Zhang et al.	Monolayer graphene	Straining sheet
		2019 [56]	Vazirisereshk et al.	Graphene, MoS ₂ and Graphene/MoS ₂ heterostructure	Low friction?
	Num.	2015 [57]	Yoon et al.	Si tip, graphene on SiO ₂	Stick-slip: tip size, scan angle, layer thickness, substrate flexibility
		2016 [58]	Li et al.	Si tip, graphene on a-Si substrate	Increasing layers
SFA	Num.	2011 [59]	Wijn et al.	Graphene flakes between graphite	Rotational dynamics, superlubricity, temperature
		2012 [22]	H. J. Kim and D. E. Kim.	Carbon sheet	Corrugated nano-structured surfaces
Flake	Exp	2005 [47]	Dienwiebel et al.	Graphene on graphite	Commensurability, superlubricity
		2013 [60]	Feng et al.	Graphene on graphite	Free sliding (relevant?)
	Num.	2009 [61]	Bonelli et al.	Graphene on graphite	Tight-binding, commensurability, load, flake size
		2012 [62]	Reguzzoni et al.	Graphene on graphite	Graphite thickness
		2014 [63]	Liu et al.	Graphene on graphite	Thickness, deformations, high speed
		2018 [64]	P. Zhu and Li	Graphene on gold	Flake size, commensurability
		2019 [65]	Zhang et al.	Graphene on diamond	Temperature, sliding angle, friction coefficient

One of the earliest tribological simulations of graphene was carried out by Bonelli et al. [61] in 2009 using a tight-binding method (excluding thermal excitations) to simulate a graphene flake on an infinite graphene sheet [52]. They implemented a FKT-like setup where each atom in the flake is coupled horizontally to a rigid support by elastic springs. They recovered the stick-slip behaviour, which is also observed in FFM setups both experimentally [55] and numerically [58][64], and they found an agreement with the qualitative observation that soft springs allow for a clean stick-slip motion while hard springs inhibit it ($\lesssim 40$ N/m). In AFM and SFA experiments, the stick-slip motion tends to transition into smooth sliding when the speed exceeds $\sim 1 \mu\text{s}$ while in MD modelling the same transition is observed in the $\sim 1 \text{ m/s}$ region [15]. This 6 order of magnitude discrepancy has been largely discussed in connection to simplifying assumptions in MD simulations.

Bonelli et al. [61] also found that commensurability, through orientation of the flake and the direction of sliding, to be of high importance for the frictional behaviour which generally aligns with the predictions of the FK type models. They confirmed qualitatively the experimental observation of superlubricity for certain incommensurable orientations as shown experimentally by Dienwiebel et al.[47] and further supported by experimental measurements of interaction energies by Feng et al. [60]. This commensurability importance is also reported for MD simulations [65][64][59]. Bonelli et al. [61] found the friction force and coefficient to be one order of magnitude higher than that of the experimental results which they attribute to the details of the numerical modelling. Generally the experimental coefficients between graphite and most materials lies in the range 0.08-0.18 [47] and while Dienwiebel et al. [47] reported a wide range of frictional forces all the way from 28 ± 16 pN to 453 ± 16 pN in a load range $\sim [-10, 20]n\text{N}$ the change in friction with applied load was as low as 0.05-0.4 % (coef. of 0.0005-0.004). This indicates an almost independent relationship between friction and load which is attributed to the lack of change in contact area.

Furthermore, Bonelli et al. [61] found friction to decrease with flake size which is mainly attributed to the idea that boundary atoms are dominant in increasing friction, but also due to their system setup decreasing the rotational freedom as size increases. However, the decreasing friction with increasing flake size is also found for the graphene on gold MD simulation [64]. This can however be attributed to commensurability as a numerical MD study of monolayer islands of krypton on copper by Reguzzoni and Righi [66] reports that the effective commensurability increase drastically below a critical flake radius on the order of 10 Å. In a numerical study by Varini et al. [67], based on Kr islands adsorbed on Pb(111), this is further elaborated as they found that finite size effects are especially important for static friction as a pinning barrier rise from the edge (preventing otherwise superlubricity due to incommensurability). They reported a relationship $F_s \sim A^{\gamma_s}$ not only sublinear $\gamma_s < 1$ but also sublinear with respect to the island perimeter $P \propto A^{1/2}$ by having $\gamma_s = 0.25$ for a hexagonal edge and $\gamma_s = 0.37$ when circular, indicating that only a subset of the edge is responsible for the pinning effect. This aligns with the general change in friction found by [64] for different flake geometries (square, triangle, circle). Additionally, Varini et al. also found the edge pinning effect to decrease with increasing temperature as the edge energy barriers are reduced. In general this aligns with the FK models prediction of a reduction of friction due to thermal activation of the atoms overcoming the energy barriers which is also in agreement with the numerical study by Wijn et al. [59].

Evolution effects, or so-called friction strengthening, is also observed experimentally by Zhang et al. [55] (only when on substrate) and numerically by Li et al. [58], meaning that the friction force increase during the initial stick-slip cycles. However, this is only found when having the graphene sheet resting on a substrate [55] opposed to a suspended sheet, and it was found to diminish when increasing the number of graphene layers stacked (graphite) [58]. In general the friction was found to decrease with increasing number of layers which is also supported by the findings in [57] but disagree with [62]?? Zhang et al. [55] additionally found that straining a suspended stretch, modulating the flexibility which consequently change the local pinning capability of the contact interface and lowers the dynamic friction. Another surface manipulating study was performed by H. J. Kim and D. E. Kim. [22] where the investigated the effects of corrugated nano-structured surfaces which altered the contact area and structural stiffness resulting in both increased and slightly decreased friction under certain load ranges.

Negative friction coefficients **TO-DO**.

The main qualitative expectations regarding our system are summarized in ??

Table 2.2: Qualitative trends

Stick slip	Generally we expect to observe periodic stick-slip motion with a period matching the lattice constant(s) involved [19]. This is however inhibited for high stiffness of the spring coupling to a driving support and at large sliding velocity.
Static friction	The static friction is highly related to the presence of stick-slip motion. The static friction is most pronounced for commensurable configurations and will decrease drastically for incommensurability. However, further reduction of static friction is expected for an increasing flake size and increasing temperature.
Commensurability	Both static and dynamic friction is expected to be highly sensitive to commensurability, through lattice spacing, orientation of the flake relative to the substrate and by the path of sliding along the substrate. By changing the spring stiffness of the coupled driving support we expect to get a response in commensurability due to a change in translational freedom.
Friction evolution (Friction strengthening)	Friction evolution is found to be present in mono layer graphene resting on a substrate, and thus we expect this to be present in our simulation setup as well.
Negative coef	TO-DO

Having considered some qualitative expectations we take a look at the quantitative expectations for the variables such as load, velocity, temperature and contact area.

The dependency on friction of normal load turns out to be a complex matter and has proven to be highly system dependent. As already mentioned, asperity theory mainly point to a sublinear relationship between friction and load, while the FK models gives no direct predictions other than this affect the energy barriers and thus phonon dissipation. Experimentally rather different trends have been observed, although the majority agree on increasing friction with increasing load [1, p. 200]. For the graphene flake Dienwiebel et al. [47] found a seemingly non-dependent relationship while, FFM study by G. Paolicelli et al. [54] found a great fit with the sublinear predictions of Maugis-Dugdale theory ($F_f \propto (F_N - F_{N,0})^{2/3}$). Here the discrepancy might lie in the difference between a spherical tip indenting the graphene sheet (matching asperity theory) as opposed to two flat graphene/graphite sheets in contact (matching FK models). However, numerical studies with graphene in contact with graphite still find both sublinear [61] and linear [65] load dependencies.

Generally a increasing logarithmic velocity dependence is found in experimental AFM studies [1, p. 201] associated to thermally activated hopping of the scanning tip. At higher velocities thermally activated processes are less important and friction becomes independent of velocity. This has been observed for Si tips and diamond, graphite and amorphous carbon surfaces with scan velocities above $1\text{ }\mu\text{/s}$. Guerra et al. [68] have studied gold clusters on graphite using MD simulations. They found a viscous friction, friction is proportional to sliding velocity, response in both low and high speed domains. However, thermal effects reversed: at low speed (diffusive) friction decreased with increased temperature while at high speed (ballistic) speed friction increases with temperature. In the MD simulations the crossover from ballistic to diffusive occur between 10 and 1 m/s.

Experimentally Zhao et al. observed in a series of AFM on MATERIAL that friction decreases strongly with temperature as $F_{\text{fric}} \propto \exp(1/T)$. This matches theoretical predictions by Krylov et al. [38] which attributes this to thermal activation inhibiting stick-slip behaviour.

Wijn et al. [59] find that friction commensurability can be lost at higher temperature (above 200K) were the found a power law behaviour $F_k \propto T^{-1.13 \pm 0.04}$.

Zhang et al. [65] found that friction increased with temperature, using a velocity of 10 m/s. Considering the findings of [68] this discrepancy might be due to low speed diffusive behaviour as opposed to high speed ballistic behaviour.

Table 2.3: Qualitative trends

Normal load	Generally an increasing friction force is expected with increasing load. Both non-dependent, sublinear and linear relationship can be expected here.
Velocity	Generally an increasing friction force is expected with increased sliding velocity. Experimental results suggest that kinetic friction goes as $F_k \propto \ln(v)$, with the expectation that friction become independent of velocity at “high” velocities above $1\text{ }\mu\text{/s}$. Numerically a viscous $F_k \propto v$ is expected for all velocity ranges.
Temperature	.

Table 2.4: Quantitative nano friction dependence on various variables. work in progress.

Variable	Dependency	Numerical studies	Experimental
Normal force F_N	$F_{\text{fric}} \propto F_N^\alpha$ $\alpha \leq 1$	Zhang et al. [65] finds a seemingly linear relationship $F_{\text{fric}} \propto F_N$ while Bonelli et al. [61] reports a sublinear relationship. The latter corresponds with that of nanosasperity simulations where Mo et al. [19], using an amorphous carbon tip on a diamond sample, also found a sublinear relationship when including adhesion and linear without adhesion.	Experimentally rather different trends have been observed, although the majority agree on increasing friction with increasing load [1, p. 200]. For the graphebne flake Dienwiebel et al. [47] found a seemingly non-dependent relationship while Feng et al. [60] did not report on this. FFM analog to the single asperity setup have yielded both linear relationship [17] (silicon tip on gold) while Schwarz et al. [69] found that FFM with well-defined spherical tips matched with theoretical results (DMT, elastic spheres pressed together [1, p. 200]), yielding a power law $F_{\text{fric}} = F_N^{2/3}$.
Velocity v	$F_{\text{fric}} \propto \ln v$ (exp.) or $F_{\text{fric}} \propto v$ (num.)	Studies of gold clusters on graphite suggest that friction is viscous, i.e. proportional to velocity [15].	Logarithmic velocity dependence of friction has been measured for nanotip friction [1, p. 201] associated to thermal activation and possibly the time available to form bond between the tip and the substrate. At higher velocities thermally activated processes are less important and friction becomes independent of velocity. This has been observed for Si tips and diamond, graphite and amorphous carbon surfaces with scan velocities above $1 \mu\text{s}$.
Temperature T	Either increase (MD) or decrease as $F_{\text{fric}} \propto \exp(1/T)$ (experimental)	Zhang et al. [65] found simply that friction increased with temperature. The [15] gold cluster on graphite study (get reference) found that the temperature dependence was dependent on velocity regime. Low speed (diffusive) friction decreases upon heating while high speed (ballistic) friction rises with temperature.	Zhao et al. [53] found $F_{\text{fric}} \propto \exp(1/T)$.
Real contact area A	$F_{\text{fric}} \propto A$	Mo et al. [19] found that $F_{\text{fric}} \propto A$ where A is the real contact area defined by atoms within chemical range. This is not studied for the case of a nanoflake where the contact area is presumably rather constant.	

2.6 Research questions

Chapter 3

Molecular Dynamics

Thanks to advances in computing algorithms and hardware the recent years has witnessed a remarkable increase in our ability to simulate tribological processes in realistic nano-frictional system [15]. A Molecular dynamics (MD) simulation can be considered as computational “experiment”. Given a set of initial conditions and a mathematically model for interatomic forces we can solve Newton’s (or equivalent) equation of motion by numerical integration [p. 303]BHUSHAN20051507. The interatomic forces are derived from interparticle interaction potentials, which is the heart of MD simulations and the specific choice of potentials can often be quite challenging.

Alternatives to the MD simulation like Ab initio methods calculate the interaction based on quantum mechanics (solving schrödinger) right?

3.1 Potentials

The potentials used in our MD simulation is mainly based on the of Li et al. [58] which have a somewhat similar MD friction simulation setup. Li et al. impose a Silicon tip on the graphene sheet supported by a Silicon substrate where we slide the whole sheet upon the substrate. Nonetheless, this serves as a good anchor for the methodology of the setup. The covalent bonds of C-C in graphene and Si-Si in the substrate is described by the Tersoff and Stillinger–Weber potentials, respectively. A typical 12-6 Lennard–Jones potential is used to describe the van der Waals adhesive interaction between graphene and the substrate.

3.1.1 General formulation of potentials (?)

On a general note we can generalize the n-body potential as the expansion in orders of participating atoms as

$$E = \sum_i V_1(\mathbf{r}_i) + \sum_{i,j} V_2(\mathbf{r}_i, \mathbf{r}_j) + \sum_{i,j,k} V_3(\mathbf{r}_i, \mathbf{r}_j, \mathbf{r}_k) + \dots,$$

where \mathbf{r}_n is the position of the n th particle and V_m is called an m -body potential [70]. The first one-body term corresponds to an external potential, followed by the two-body term, the three-body term and so on. The simplest model that includes particle interaction is the pair potential truncating the expansion after the two-body term. A general feature of the pair potentials is that they favor close-packed structures which is unsuited to describe covalent bonds that take more open structures. In particular, pair potentials are completely inapplicable to strongly covalent systems [70]. In order to accomodate the description of covalent bonds the natural step is thus to include the next step of the expansion, the three-body terms, as we will see for the modeling of the C-C bonds in the graphene sheet and the Si-Si bonds in Silicon substrate. For the interaction between the sheet and the substrate we use a Lennard Jones pair potential describing the non-bonded van der Waals interaction. This simple interaction model between the moving object and substrate has come to be the standard in friction simulations [64], [71], [57], [3].

3.1.2 Lennard Jones

TODO: Add potential curve figure

This sections is based on [72], [73], [74].

The Lennard-Jones (LJ) model is probably one of the most famous pair potentials used in MD simulations. LJ models the potential energy between two non-bonding atoms solely based on interatomic distance. The model accounts for attractive forces arising from dipole-dipole, dipole-induced dipole and London interactions, and repulsive forces that capture the hard core of overlapping wave functions at small distances (**double check this statement**). Thus, it assumes neutrally charged atoms and was originally proposed for noble gases. The classical 12-6 version of the model (referring to the power law of the repulsive and attractive forces respectively) reads

$$E = 4\epsilon \left[\left(\frac{\sigma}{r} \right)^{12} - \left(\frac{\sigma}{r} \right)^6 \right], \quad r < r_c, \quad (3.1)$$

where r is the interatomic distance with cut-off r_c , ϵ is the depth of the potential well and σ the interatomic distance where the potential is zero. By solving for the potential minimum ($dE/dr = 0$) we find the equilibrium distance to be $r_0 = \sigma 2^{1/6}$. This makes for a slightly more intuitive interpretation of σ which effectively sets the equilibrium distance between atoms, i.e. the dividing line for which the force is repulsive or attractive.

3.1.3 Stillinger weber

TODO: Add potential figure and or figure illustrating three body angles.

This section is based on [[75], [76]]

The stillinger weber potential takes the form of a three body potential

$$E = \sum_i \sum_{j>i} \phi_2(r_{ij}) + \sum_i \sum_{j \neq i} \sum_{k>j} \phi_3(r_{ij}, r_{ik}, \theta_{ijk}),$$

where r_{ij} denotes the distance between atom i and j and θ_{ijk} the angle between bond ij and jk . The summations is over all neighbours j and k of atom i within a cut-off distance $r = a\sigma$.

The two-body term ϕ_2 builds from the LJ model with the addition of an exponential cutoff term

$$\phi_2(r_{ij}) = A_{ij}\epsilon_{ij} \left[B_{ij} \left(\frac{\sigma_{ij}}{r_{ij}} \right)^{p_{ij}} - \left(\frac{\sigma_{ij}}{r_{ij}} \right)^{q_{ij}} \right] \exp\left(\frac{\sigma_{ij}}{r_{ij} - a_{ij}\sigma_{ij}}\right). \quad (3.2)$$

The model parameters A , ϵ , B , σ , p , q and a comes with i, j indices to indicate that these parameters should be specified for each unique pair of atom types. However, in our case we will only provide a single value for each model parameter as we are exclusively dealing with Si-Si bonds. We see that the first term in Eq. (3.2) is reminiscent of the LJ model in Eq. (3.1) while the last term effectively drives the potential to zero at $r = a\sigma$, which is thus the chosen cut-off distance for the potential evaluation. With the model parameters for the Si-Si modelling (see Table 3.1) the cut-off becomes ~ 3.8 Å.

The three body term includes an angle dependency as

$$\phi_3(r_{ij}, r_{ik}, \theta_{ijk}) = \lambda_{ijk} \epsilon_{ijk} \left[\cos \theta_{ijk} - \cos \theta_{0,ijk} \right]^2 \exp\left(\frac{\gamma_{ij}\sigma_{ij}}{r_{ij} - a_{ij}\sigma_{ij}}\right) \exp\left(\frac{\gamma_{ik}\sigma_{ik}}{r_{ik} - a_{ik}\sigma_{ik}}\right), \quad (3.3)$$

where $\theta_{0,ijk}$ is the equilibrium angle. The first term of Eq. (3.3) includes an angle dependency analog to a harmonic oscillator based on a cosine angle distance from the equilibrium angle. The final two terms act again as a cut-off function by driving the potential to zero at $r_{ij} = a_{ij}\sigma_{ij}$ and $r_{ik} = a_{ik}\sigma_{ik}$ respectively.

The parameters used for the Si-Si bond modeling is displayed in Table 3.1 along with an interpretation of each model parameter.

Table 3.1: Parameters for the stilliner weber potential used for intermolecular interactions in the silicon substrate.

Parameter	Value	Description
ϵ	2.1683	Individual depth of the potential well for each atom type pair/tiplets.
σ	2.0951	Distance for which the individual pair interactions has zero potential (analog to the LJ model).
a	1.80	The individual cut-off distance for each atom type pair.
λ	21.0	The overall depth of the three-body potential well.
γ	1.20	The shape of the three-body cut-off terms.
$\cos(\theta_0)$	-1/3	Cosine of equilibrium angle.
A	7.049556277	The overall depth of the two-body potential well.
B	0.6022245584	Scales the repulsion part of the two-body term.
p	4.0	The power dependency for the repulsion part of the two-body term.
q	0.0	The power dependency for the attraction part of the two-body term.
tol	0.0	LAMMPS: Option to define a different cut-off than the theoretical of $r = a\sigma$. $tol = 0$ refers to the theoretical being used.

3.1.4 Tersoff

This section is based on [[77], [70]].

The tersoff potential abandon the idea of a general n -body form and attempts instead to build the model on a more physics informed approach; The more neighbours an atom has the weaker the bonds will be. Thus it introduces the bond order (bond strength), that is environment specific and decrease with increasing bond coordination (number of neighbours for a given atom). The potential energy is taken to have the form

$$E = \sum_i E_i = \frac{1}{2} \sum_{i \neq j} V_{ij},$$

$$V_{ij} = f_C(r_{ij}) [f_R(r_{ij}) + b_{ij} f_A(r_{ij})],$$

where the total potential energy is decomposed into a bond energy V_{ij} . The indices i and j run over the atoms of the system with r_{ij} denoting the distance between atom i and j . Notice that the sum includes all combinations of i, j where $i \neq j$ meaning that the same bond is double counted which is the reason for the additional factor 1/2. The reasoning behind comes from the asymmetry of the bond order $b_{ij} \neq b_{ji}$ leading to a $V_{ij} \neq V_{ji}$. The bond energy is composed of a repulsive term f_R , arising from overlapping wave functions, and an attractive term f_A associated with bonding. f_C is simply a smooth cut-off function to increase computational efficiency. b_{ij} represent the bond order, i.e. the strength of the bonds, which depends inversely on the number of bonds, the bond angles (θ_{ijk}) and optionally the relative bonds lengths (r_{ij}, r_{jk}). Notice that an additional cut-off term a_{ij} was originally multiplied to f_R as a way of including terms that limit the range of the interactions to the first neighbour shell. These kind of limitations is already included in b_{ij} for the attractive term f_A but is often omitted for the repulsive term f_R , and we do so to by setting $a_{ij} = 1$.

The cut-off function f_C goes from 1 to 0 over a small interval range $R \pm D$ as

$$f_C(r) = \begin{cases} 1 & r < R - D \\ \frac{1}{2} - \frac{1}{2} \sin\left(\frac{\pi}{2} \frac{r-R}{D}\right) & R - D < r < R + D \\ 0 & r > R + D \end{cases}$$

which is continuous and differentiable for all r . R is usually chosen to include only the first neighbour shell. The repulsive and attractive terms f_R and f_A is modelled as an exponential function, similar to a morse potential,

$$f_R(r) = A \exp(-\lambda_1 r),$$

$$f_A(r) = -B \exp(-\lambda_2 r).$$

The novel feature of the model lies in modeling of the bond order b_{ij} which includes three-body interactions by summing over a third atom $k \neq i, j$ within the cut-off $r_{ik} < R + D$ as shown in the following.

$$b_{ij} = (1 + \beta^n \zeta_{ij}^n)^{-\frac{1}{2n}} \quad (3.4)$$

$$\zeta_{ij} = \sum_{k \neq i, j} f_C(r_{ik}) g(\theta_{ijk}(r_{ij}, r_{ik})) \exp(\lambda_3^m (r_{ij} - r_{ik})^m) \quad (3.5)$$

$$g(\theta) = \gamma_{ijk} \left(1 + \frac{c^2}{d^2} - \frac{c^2}{[d^2 + (\cos \theta - \cos \theta_0)^2]} \right). \quad (3.6)$$

In Eq. (3.6) $\zeta_{i,j}$ is an effective coordination and $g(\theta)$ captures angle dependency as it is minimized at the equilibrium angle $\theta = \theta_0$.

The parameters used to model the graphene C-C bonds is summarized in Table 3.2

Table 3.2: Parameters for the tersoff potential used for intermolecular interations in the graphene sheet

Parameter	Value	Description
m	3.0	Default (not used since $\lambda_3 = 0$)
γ	1.0	...
λ_3	0.0 \AA^{-1}	...
c	3.8049×10^4	Strength of the angular effect
d	4.3484	Determines the “sharpness” of the angular dependency
$\cos(\theta_0)$	-0.57058	Cosine of the equilibrium angle
n	0.72751	Power law exponent for the bond order dependency
β	1.5724×10^{-7}	...
λ_2	2.2119 \AA^{-1}	Decay of repulsion potential term
B	346.74 eV	Attractive potential term minimum at core ($r_{ij} = 0$).
R	1.95 Å	Center distance for cut-off
D	0.15 Å	Thickness of cut-off layers
λ_1	3.4879 \AA^{-1}	Decay of repulsion potential term
A	1393.6 eV	Repulsion potential term at core ($r_{ij} = 0$)

3.2 Integration

Having defined a system of particles governed by interatomic potentials we need to move the system forward in time. By solving Newtons equations of motion we effectively sample the microcanonical ensemble characterized by a constant number of particles N , volume V and energy E , hence denoted NVE. Newtons equaitons of motion read

$$m_i \frac{d^2 \mathbf{r}_i}{dt^2} = \mathbf{F}_i = -\nabla U_i \quad (3.7)$$

where i is the particle index and m_i its mass, $\mathbf{r}_i = (x_i, y_i, z_i)$ the position, t is time, $\nabla_i = (\frac{\partial}{\partial x_i}, \frac{\partial}{\partial y_i}, \frac{\partial}{\partial z_i})$ and U_i the potential energy. The potential energy is a function of the particle positions of nearby particles depending on the specefic potential in use. Since the forces defined by the potentials is conservative we expect the energy of the solution to be conserved. We can redefine Eq. (3.7) in terms of two coupled first order differential equations

$$\dot{\mathbf{v}}_i(t) = \frac{\mathbf{F}}{m_i}, \quad \dot{\mathbf{r}}_i(t) = \mathbf{v}_i(t), \quad (3.8)$$

where $\dot{x} = dx/dt$ (Newton's notation) and $\mathbf{v} = (v_x, v_y, v_z)$ is velocity. Numerically we can solve the coupled equations by integrating over discrete timesteps. That is, we discretize the solution into temporal steps $t_k = t_0 + k\Delta t$ with start time t_0 and time-step Δt .

3.2.1 Velocity Verlet

A common algorithm to integrate Newton's equation of motion (as formulated in Eq. (3.8)) is the *velocity verlet*. We can derive the algorithm by the use of Taylor expansions. We begin by expanding the next-step position vector $\mathbf{r}_i(t + \Delta t)$ at time t

$$\mathbf{r}_i(t + \Delta t) = \mathbf{r}_i(t) + \dot{\mathbf{r}}_i(t)\Delta t + \frac{\ddot{\mathbf{r}}_i(t)}{2}\Delta t^2 + \mathcal{O}(\Delta t^3), \quad (3.9)$$

where $\ddot{\mathbf{r}} = d^2\mathbf{r}/dt^2$ and Δt^n is simply the relaxed notation for $(\Delta t)^n$. Similar we take the expansions of the next-step velocity vector $\mathbf{v}_i(t + \Delta t)$ at time t

$$\mathbf{v}_i(t + \Delta t) = \mathbf{v}_i(t) + \dot{\mathbf{v}}_i(t)\Delta t + \frac{\ddot{\mathbf{v}}_i(t)}{2}\Delta t^2 + \mathcal{O}(\Delta t^3). \quad (3.10)$$

Finally, by taking the expansion of $\dot{\mathbf{v}}_i(t + \Delta t)$ we can eliminate the $\ddot{\mathbf{v}}_i$ -term in Eq. (3.10) and simplify it as shown in the following.

$$\begin{aligned} \dot{\mathbf{v}}_i(t + \Delta t) &= \dot{\mathbf{v}}_i(t) + \ddot{\mathbf{v}}_i(t)\Delta t + \mathcal{O}(\Delta t^2) \\ \frac{\ddot{\mathbf{v}}_i(t)}{2}\Delta t^2 &= \frac{\Delta t}{2}(\dot{\mathbf{v}}(t + \Delta t) - \dot{\mathbf{v}}_i(t)) + \mathcal{O}(\Delta t^3) \\ &\Downarrow \\ \mathbf{v}_i(t + \Delta t) &= \mathbf{v}_i(t) + \dot{\mathbf{v}}_i(t)\Delta t + \frac{\Delta t}{2}(\dot{\mathbf{v}}_i(t + \Delta t) - \dot{\mathbf{v}}_i(t)) + \mathcal{O}(\Delta t^3) \\ &= \mathbf{v}_i(t) + \frac{\Delta t}{2}(\dot{\mathbf{v}}_i(t) + \dot{\mathbf{v}}_i(t + \Delta t)) + \mathcal{O}(\Delta t^3). \end{aligned} \quad (3.11)$$

By combining Eq. (3.9) and Eq. (3.11) and using Newton's second equation $\dot{\mathbf{v}} = \mathbf{F}_i(t)/m_i$ and $\mathbf{v} = \dot{\mathbf{r}}$ we arrive at the final scheme

$$\begin{aligned} \mathbf{r}_i(t + \Delta t) &= \mathbf{r}_i(t) + \mathbf{v}_i(t)\Delta t + \frac{\mathbf{F}_i(t)}{2m_i}\Delta t^2 + \mathcal{O}(\Delta t^3), \\ \mathbf{v}_i(t + \Delta t) &= \mathbf{v}_i(t) + \frac{\mathbf{F}_i(t) + \mathbf{F}_i(t + \Delta t)}{2m_i}\Delta t + \mathcal{O}(\Delta t^3). \end{aligned}$$

The scheme will give a local error of order Δt^3 corresponding to a global error of Δt^2 . One of the most popular ways to implement this numerically is as stated in the following steps.

1. Calculate $v_{k+\frac{1}{2}} = v_k + \frac{F_k}{2m}\Delta t$.
2. Calculate $r_{k+1} = r_k + v_{k+\frac{1}{2}}\Delta t$.
3. Evaluate the force $F_{k+1} = F(r_{k+1})$.
4. Calculate $v_{k+1} = v_{k+\frac{1}{2}} + \frac{F_{k+1}}{2m}\Delta t$

3.3 Thermostats

As we already mentioned above in Sec. 2, any kind of sliding friction involves mechanical work, some of which is then transformed into heat (the rest going into structural transformations, wear, etc.). The heat is then transported away by phonons (and electrons in the case of metallic sliders) and eventually dissipated to the environment [15].

Likewise all excitations generated in the simulations should be allowed to propagate in the system and disperse in the bulk of both sheet and substrate. Due to small simulation size these is likely to reflect back

and ‘‘pile up’’ unphysically. Thus in order to avoid continuous heating and attain a steady state the (Joule) heat must be removed at a steady state. This is very the viscous damping of the Langevin equations enter the picture. It can be difficult to set the value γ for the magnitude of this damping. The unphysical introduction of heat sink can be mitigated by some modifications he mention, which is kind of next level I guess.

3.3.1 Langevin thermostat

In order to control the temperature of the system we introduce the so-called Langevin thermostat. This is a stochastic thermostat that modifies Newton's equation of motion such that solution lies in the canonical ensemble characterized by a constant number of particles N , constant volume V and constant temperature T , hence denoted NVT. The canonical ensemble system is represented by the finite system being in contact with an infinite heat bath of temperature T . The NVT ensemble is equivalent to sampling a system in thermodynamic equilibrium where the weight of each microscopic state is given by the Boltzmann factor $\exp[-E/(k_B T)]$.

The Langevin equation is the modified version of Newton's second law for a Brownian particle. A Brownian particle is a small particle suspended in liquid, e.g. pollen or dust, named after Robert Brown (1773–1858) who was the first to observe its jittery motion. The Langevin equation describes this motion as the combination of viscous drag force $-\gamma \mathbf{v}$, where γ is a positive friction coefficient and \mathbf{v} the velocity vector, and a random fluctuation force \mathbf{R} . The Langevin equation reads

$$m \frac{d\mathbf{v}}{dt} = -\gamma \mathbf{v} + \mathbf{R} \quad (3.12)$$

where m is the particle mass. This effectively describes the particle of interest, the Brownian particle, as being suspended in a sea of smaller particles. The collision with these smaller particles is modelled by the drag force and the fluctuation force. We notice that if the fluctuation force is excluded Eq. (3.12) becomes

$$m \frac{d\mathbf{v}}{dt} = -\gamma \mathbf{v} \Rightarrow \mathbf{v}_i(t) = v(0) e^{-\frac{\gamma t}{m}},$$

where the solution shows that the Brownian particle will come to a complete stop after a long time $\mathbf{v}_i(t \rightarrow \infty) \rightarrow \mathbf{0}$. This is in violation with the equipartition theorem

$$\frac{1}{2} m \langle v^2 \rangle_{eq} = \frac{k_B T}{2},$$

and hence the fluctuation force is necessary to obtain the correct equilibrium.

The following calculations are done in one dimension in order to simplify the notation. We describe the statistical nature of the collisions as a sum of independent momentum transfers

$$\Delta P = \sum_i^N \delta p_i$$

where ΔP denotes the change of momentum after N momentum transfers δp_i from the environment to the Brownian particle. We assume the first and second moments $\langle \delta p \rangle = 0$ and $\langle \delta p^2 \rangle = \sigma^2$. When N is large the central limit theorem states that the random variable ΔP has a Gaussian distribution with $\langle P \rangle = 0$ and $\langle \Delta P^2 \rangle = N\sigma^2$. If we consider the momentum change ΔP over a discrete time Δt , where the number of collisions is proportional to time $N \propto \Delta t$, the corresponding fluctuation force $R = \Delta P / \Delta t$ will have a variance

$$\langle R^2 \rangle = \frac{\langle \Delta P^2 \rangle}{\Delta t^2} = \frac{N\sigma^2}{\Delta t^2} \propto \frac{1}{\Delta t}.$$

In a computer simulation we need to pick a random force $R(t)$ from a Gaussian distribution every time-step Δt . These forces will not be correlated as long as Δt is larger than the correlation time of the forces from the molecules which we will assume for this model (I think there exist corrections for this to refer to here). With this assumption we can write the correlation function as

$$\langle R(t) R(0) \rangle = \begin{cases} \frac{a}{\Delta t}, & |\Delta t| < \Delta t/2 \\ 0, & |\Delta t| > \Delta t/2, \end{cases} \quad (3.13)$$

where a is some strength of (...?). In the limit $\Delta t \rightarrow 0$ the correlation function becomes

$$\langle R(t)R(0) \rangle = a\delta(t), \quad (3.14)$$

where δ denotes the dirac delta function. This is valid for all spatial coordinates which will all be independent of each other. Since both the drag force and the fluctuation force originate from the molecular fluid, where the drag force $-\alpha v$ is velocity dependent it is reasonable to assume that fluctuation force is independent of velocity, i.e. $\langle R_i v_j \rangle = 0$ for all cartesian indices i and j .

In the following we will attempt justify the Langevin equaiton (why it is like it is) and determine the relationship between the drag coefficient γ and the random force R .

From the Langevin equation Eq. (3.12) we can compute the velocity autocorrelation function (Move to appendix?). We do this in one dimension for simplicity. We begin by multiplying by $(e^{\gamma t/m})/m$

$$\dot{v}(t)e^{\gamma t/m} + \frac{\gamma}{m}v(t)e^{\frac{\gamma t}{m}} = \frac{F}{m}e^{\frac{\gamma t}{m}},$$

and integrate from $t = -\infty$. By the use of integration by parts on the latter term on the left hand side we calculate the velocity

$$\begin{aligned} \int_{-\infty}^t dt' \dot{v}(t')e^{\frac{\gamma t'}{m}} + \frac{\gamma}{m}v(t)e^{\frac{\gamma t}{m}} &= \int_{-\infty}^t dt' e^{\frac{\gamma t'}{m}} \frac{F(t')}{m} \\ \int_{-\infty}^t dt' \dot{v}(t')e^{\frac{\gamma t'}{m}} + \left(\left[v(t')e^{\frac{\gamma t'}{m}} \right]_{-\infty}^t - \int_{-\infty}^t dt' \dot{v}(t')e^{\frac{\gamma t'}{m}} \right) &= \int_{-\infty}^t dt' e^{\frac{\gamma t'}{m}} \frac{F(t')}{m} \\ v(t) &= \int_{-\infty}^t dt' e^{\frac{-\gamma(t-t')}{m}} \frac{F(t')}{m}, \end{aligned}$$

where $e^{\frac{-\gamma t}{m}}$ plays the role of a response function. We can then calculate the autocorrelation

$$\begin{aligned} \langle v(t)v(0) \rangle &= \int_{-\infty}^t dt_1 \int_{-\infty}^0 dt_2 e^{\frac{t-t_1-t_2}{m}} \frac{\langle F(t_1)F(t_2) \rangle}{m^2} \\ &= \int_{-\infty}^t dt_1 \int_{-\infty}^0 dt_2 e^{\frac{t-t_1-t_2}{m}} \frac{a\delta(t_1-t_2)}{m^2} \\ &= \int_{-\infty}^0 dt_2 e^{\frac{t-2t_2}{m}} \frac{a}{m^2} = \frac{a}{2m\gamma} e^{-\frac{\gamma t}{m}}, \end{aligned}$$

where we used Eq. (3.14) and the fact that the integration commutes with the average (we are allowed to flip the order). By comparing this with the equipartition theorem we get

$$\begin{aligned} \frac{1}{2}m\langle v^2 \rangle &= \frac{k_B T}{2} \\ \frac{1}{2}m\langle v(0)v(0) \rangle &= \frac{a}{4\gamma} = \frac{k_B T}{2} \\ a &= 2\gamma k_B T \end{aligned}$$

We notice the appereance of γ meaning that the magnitude of the fluctuations increase both with friction and temperature. Further we can integrate the velocity over time to get displacement $x(t)$ and show that the variance (show this? In appendix maybe?) is

$$\langle x^2(t) \rangle = \frac{2k_B T}{\gamma} \left(t - \frac{m}{\gamma} \left(1 - e^{-\gamma t/m} \right) \right),$$

where for $t \gg m/\gamma$ only the t -term survies yielding

$$\langle x^2(t) \rangle = 2k_B T t / \gamma.$$

In 1D, the diffusion constant D is related to the variance as $\langle x^2 \rangle = 2Dt$, meaning that this represents the einstein relation $D = \mu k_B T$ with the mobility $\mu = 1/\gamma$.

when $t \ll m/\gamma$ we use the Taylor expansion $1 - e^{-x} \approx x - x^2/2$ for $x \ll 1$ to get

$$\langle x^2(t) \rangle = \frac{k_B T}{m} t^2$$

which exactly matches the thermal velocity

$$v_{\text{th}} \frac{\langle x^2(t) \rangle}{t^2} = \frac{k_B T}{m}$$

which follows from the equipartition theorem. The finite correlation time γ/m hence describe the crossover from the ballistic regime $\sqrt{\langle x^2(t) \rangle} \propto t$ to the diffusive regime $\sqrt{\langle x^2(t) \rangle} \propto \sqrt{t}$.

Introduce the fluctuation-dissipation theorem concept earlier since this is a motivaiton for the Langeivn equation.

3.3.2 Implementing Langevin

The implementation of the Langevin equation into LAMMPS follows [78] and updates the force vector for each particle as

$$\begin{aligned} \mathbf{F} &= \mathbf{F}_c + \mathbf{F}_f + \mathbf{F}_r \\ &= -\nabla U - \gamma m \mathbf{v} + \sqrt{\frac{2k_B T m \gamma}{\Delta t}} \mathbf{h}(t) \end{aligned} \quad (3.15)$$

where \mathbf{F}_c is the conservative force computed via the usual inter-particle interactions described by the potential U , \mathbf{F}_f is the drag force and \mathbf{F}_r is the random fluctuation force where \mathbf{h} is a random vector drawn from a normal distribution with zero mean and unit variance. Notice that this generalized description of the Langevin equation deviates from the presentation in Eq. (3.12) since we have added the conservative force \mathbf{F}_c , but also by the appearance of the mass in both the drag force and the fluctuation force due to the introduction of damping. It is beyond out scope to comprehend this. However, the fact that Δt now appears in the denominator for the random force variance $2k_B T m \gamma / \Delta t$ is due to the fact that we have discretized time. This in agreement with the formulation in Eq. (3.13). By applying Eq. (3.15) we get the refined velocity verlet scheme

$$\begin{aligned} \mathbf{v}_i(t + \Delta t/2) &= \mathbf{v}_i(t) - \frac{\Delta t}{2} \left(\frac{\nabla_i U(t)}{m_i} + \gamma \mathbf{v}_i \right) + \sqrt{\frac{k_B T \gamma \Delta t}{2m_i}} \mathbf{h}_i \\ \mathbf{r}_i(t + \Delta t) &= \mathbf{r}_i(t) + \mathbf{v}_i(t + \Delta t/2) \Delta t \\ \mathbf{v}_i(t + \Delta t) &= \mathbf{v}_i(t + \Delta t/2) - \frac{\Delta t}{2} \left(\frac{\nabla_i U(t + \Delta t)}{m_i} + \gamma \mathbf{v}_i(t + \Delta t/2) \right) + \sqrt{\frac{k_B T \gamma \Delta t}{2m_i}} \mathbf{h}_i \end{aligned}$$

with new random vector \mathbf{h}_i for each particle and each update. Notice however, that LAMMPS only apply this scheme to the particle groups with the thermostat on.

3.4 MD limitations (?)

3.5 LAMMPS

Part II

Simulations

Appendices

Appendix A

Appendix B

Appendix C

Bibliography

- ¹E. Gnecco and E. Meyer, *Elements of friction theory and nanotribology* (Cambridge University Press, 2015).
- ²Bhusnur, “Introduction”, in *Introduction to tribology* (John Wiley & Sons, Ltd, 2013) Chap. 1, 1–?
- ³H.-J. Kim and D.-E. Kim, “Nano-scale friction: a review”, *International Journal of Precision Engineering and Manufacturing* **10**, 141–151 (2009).
- ⁴K. Holmberg and A. Erdemir, “Influence of tribology on global energy consumption, costs and emissions”, *Friction* **5**, 263–284 (2017).
- ⁵B. Bhushan, “Gecko feet: natural hairy attachment systems for smart adhesion – mechanism, modeling and development of bio-inspired materials”, in *Nanotribology and nanomechanics: an introduction* (Springer Berlin Heidelberg, Berlin, Heidelberg, 2008), pp. 1073–1134.
- ⁶P. Z. Hanakata, E. D. Cubuk, D. K. Campbell, and H. S. Park, “Accelerated search and design of stretchable graphene kirigami using machine learning”, *Phys. Rev. Lett.* **121**, 255304 (2018).
- ⁷P. Z. Hanakata, E. D. Cubuk, D. K. Campbell, and H. S. Park, “Forward and inverse design of kirigami via supervised autoencoder”, *Phys. Rev. Res.* **2**, 042006 (2020).
- ⁸L.-K. Wan, Y.-X. Xue, J.-W. Jiang, and H. S. Park, “Machine learning accelerated search of the strongest graphene/h-bn interface with designed fracture properties”, *Journal of Applied Physics* **133**, 024302 (2023).
- ⁹Y. Mao, Q. He, and X. Zhao, “Designing complex architectured materials with generative adversarial networks”, *Science Advances* **6**, eaaz4169 (2020).
- ¹⁰Z. Yang, C.-H. Yu, and M. J. Buehler, “Deep learning model to predict complex stress and strain fields in hierarchical composites”, *Science Advances* **7**, eabd7416 (2021).
- ¹¹A. E. Forte, P. Z. Hanakata, L. Jin, E. Zari, A. Zareei, M. C. Fernandes, L. Sumner, J. Alvarez, and K. Bertoldi, “Inverse design of inflatable soft membranes through machine learning”, *Advanced Functional Materials* **32**, 2111610 (2022).
- ¹²S. Chen, J. Chen, X. Zhang, Z.-Y. Li, and J. Li, “Kirigami/origami: unfolding the new regime of advanced 3D microfabrication/nanofabrication with “folding””, *Light: Science & Applications* **9**, 75 (2020).
- ¹³Z. Deng, A. Smolyanitsky, Q. Li, X.-Q. Feng, and R. J. Cannara, “Adhesion-dependent negative friction coefficient on chemically modified graphite at the nanoscale”, *Nature Materials* **11**, 1032–1037 (2012).
- ¹⁴R. W. Liefferink, B. Weber, C. Coulais, and D. Bonn, “Geometric control of sliding friction”, *Extreme Mechanics Letters* **49**, 101475 (2021).
- ¹⁵N Manini, O. M. Braun, E Tosatti, R Guerra, and A Vanossi, “Friction and nonlinear dynamics”, *Journal of Physics: Condensed Matter* **28**, 293001 (2016).
- ¹⁶B. Bhushan and A. V. Kulkarni, “Effect of normal load on microscale friction measurements”, *Thin Solid Films* **278**, 49–56 (1996).
- ¹⁷J. Gao, W. D. Luedtke, D. Gourdon, M. Ruths, J. N. Israelachvili, and U. Landman, “Frictional forces and amontons’ law: from the molecular to the macroscopic scale”, *The Journal of Physical Chemistry B* **108**, Publisher: American Chemical Society, 3410–3425 (2004).
- ¹⁸J. H. Dieterich, “Time-dependent friction in rocks”, *Journal of Geophysical Research (1896-1977)* **77**, 3690–3697 (1972).
- ¹⁹Y. Mo, K. T. Turner, and I. Szlufarska, “Friction laws at the nanoscale”, *Nature* **457**, 1116–1119 (2009).

- ²⁰G. Carbone and F. Bottiglione, “Asperity contact theories: do they predict linearity between contact area and load?”, *Journal of the Mechanics and Physics of Solids* **56**, 2555–2572 (2008).
- ²¹F. Bowden and D. Tabor, *The friction and lubrication of solids*, International series of monographs on physics vb. 1 (Clarendon Press, 2001).
- ²²H.-J. Kim and D.-E. Kim, “Molecular dynamics simulation of atomic-scale frictional behavior of corrugated nano-structured surfaces”, *Nanoscale* **4**, 3937–3944 (2012).
- ²³W. Commons, *File:asperities.svg — wikimedia commons, the free media repository*, [Online; accessed 3-February-2023], 2022.
- ²⁴I. Szlufarska, M. Chandross, and R. W. Carpick, “Recent advances in single-asperity nanotribology”, *Journal of Physics D: Applied Physics* **41**, 123001 (2008).
- ²⁵G. Binnig, C. F. Quate, and C. Gerber, “Atomic force microscope”, *Phys. Rev. Lett.* **56**, 930–933 (1986).
- ²⁶S. S. Perry, “Scanning Probe Microscopy Measurements of Friction”, *MRS Bulletin* **29**, 478–483 (2004).
- ²⁷Hertz, “On the contact of elastic solids”, *Crelle’s Journal* **92**, 156–171.
- ²⁸D. Maugis, “Adhesion of spheres: the jkr-dmt transition using a dugdale model”, *Journal of Colloid and Interface Science* **150**, 243–269 (1992).
- ²⁹M. H. Müser, “Rigorous field-theoretical approach to the contact mechanics of rough elastic solids”, *Phys. Rev. Lett.* **100**, 055504 (2008).
- ³⁰B. N. J. Persson, “Theory of rubber friction and contact mechanics”, *The Journal of Chemical Physics* **115**, 3840–3861 (2001).
- ³¹J. A. Greenwood and J. B. P. Williamson, *Contact of nominally flat surfaces*, en, 1966.
- ³²A. Bush, R. Gibson, and T. Thomas, “The elastic contact of a rough surface”, *Wear* **35**, 87–111 (1975).
- ³³B. Luan and M. O. Robbins, “The breakdown of continuum models for mechanical contacts”, *Nature* **435**, 929–932 (2005).
- ³⁴Y. Dong, A. Vadakkepatt, and A. Martini, “Analytical models for atomic friction”, *Tribology Letters* **44**, 10.1007/s11249-011-9850-2 (2011).
- ³⁵E. Gnecco, R. Bennewitz, T. Gyalog, C. Loppacher, M. Bammerlin, E. Meyer, and H.-J. Güntherodt, “Velocity dependence of atomic friction”, *Phys. Rev. Lett.* **84**, 1172–1175 (2000).
- ³⁶P. Hänggi, P. Talkner, and M. Borkovec, “Reaction-rate theory: fifty years after kramers”, *Rev. Mod. Phys.* **62**, 251–341 (1990).
- ³⁷Y. Sang, M. Dubé, and M. Grant, “Thermal effects on atomic friction”, *Phys. Rev. Lett.* **87**, 174301 (2001).
- ³⁸S. Y. Krylov, K. B. Jinesh, H. Valk, M. Dienwiebel, and J. W. M. Frenken, “Thermally induced suppression of friction at the atomic scale”, *Phys. Rev. E* **71**, 065101 (2005).
- ³⁹S. Krylov and J. Frenken, “Thermal contact delocalization in atomic scale friction: a multitude of friction regimes”, *English, New Journal of Physics* **9**, 10.1088/1367-2630/9/10/398 (2007).
- ⁴⁰K. B. Jinesh, S. Y. Krylov, H. Valk, M. Dienwiebel, and J. W. M. Frenken, “Thermolubricity in atomic-scale friction”, *Phys. Rev. B* **78**, 155440 (2008).
- ⁴¹Q. Li, Y. Dong, D. Perez, A. Martini, and R. W. Carpick, “Speed dependence of atomic stick-slip friction in optimally matched experiments and molecular dynamics simulations”, *Phys. Rev. Lett.* **106**, 126101 (2011).
- ⁴²Y. Dong, Q. Li, and A. Martini, “Molecular dynamics simulation of atomic friction: a review and guide”, *Journal of Vacuum Science & Technology A* **31**, 030801 (2013).
- ⁴³K. Johnson and J. Woodhouse, “Stick-slip motion in the atomic force microscope”, *Tribology Letters* **5**, 155–160 (1998).
- ⁴⁴S. N. Medyanik, W. K. Liu, I.-H. Sung, and R. W. Carpick, “Predictions and observations of multiple slip modes in atomic-scale friction”, *Phys. Rev. Lett.* **97**, 136106 (2006).
- ⁴⁵J. Frenkel and T. Kontorova, “On the theory of plastic deformation and twinning”, *Phys. Z. Soviet.* **13** (1938).
- ⁴⁶J. Norell, A. Fasolino, and A. Wijn, “Emergent friction in two-dimensional fренkel-kontorova models”, *Physical Review E* **94**, 10.1103/PhysRevE.94.023001 (2016).

- ⁴⁷M. Dienwiebel, N. Pradeep, G. S. Verhoeven, H. W. Zandbergen, and J. W. Frenken, “Model experiments of superlubricity of graphite”, *Surface Science* **576**, 197–211 (2005).
- ⁴⁸C. Kittel, *Introduction to solid state physics*, 8th ed. (Wiley, 2004).
- ⁴⁹J. A. van den Ende, A. S. de Wijn, and A. Fasolino, “The effect of temperature and velocity on superlubricity”, *Journal of Physics: Condensed Matter* **24**, 445009 (2012).
- ⁵⁰M. Weiss and F.-J. Elmer, “Dry friction in the Frenkel-Kontorova-Tomlinson model: dynamical properties”, *Zeitschrift für Physik B Condensed Matter* **104**, 55–69 (1997).
- ⁵¹B. Bhushan, “Nanotribology and nanomechanics”, *Wear* **259**, 15th International Conference on Wear of Materials, 1–? (2005).
- ⁵²O. Penkov, H.-J. Kim, H.-J. Kim, and D.-E. Kim, “Tribology of graphene: A review”, *International Journal of Precision Engineering and Manufacturing* **15**, 577–585 (2014).
- ⁵³X. Zhao, M. Hamilton, W. G. Sawyer, and S. S. Perry, “Thermally activated friction”, *Tribology Letters* **27**, 113–117 (2007).
- ⁵⁴G Paolicelli, M Tripathi, V Corradini, A Candini, and S Valeri, “Nanoscale frictional behavior of graphene on sio₂ and ni(111) substrates”, *Nanotechnology* **26**, 055703 (2015).
- ⁵⁵S. Zhang, Y. Hou, S. Li, L. Liu, Z. Zhang, X.-Q. Feng, and Q. Li, “Tuning friction to a superlubric state via in-plane straining”, *Proceedings of the National Academy of Sciences* **116**, Publisher: Proceedings of the National Academy of Sciences, 24452–24456 (2019).
- ⁵⁶M. R. Vazirisereshk, H. Ye, Z. Ye, A. Otero-de-la Roza, M.-Q. Zhao, Z. Gao, A. T. C. Johnson, E. R. Johnson, R. W. Carpick, and A. Martini, “Origin of nanoscale friction contrast between supported graphene, mos₂, and a graphene/mos₂ heterostructure”, *Nano Letters* **19**, PMID: 31267757, 5496–5505 (2019).
- ⁵⁷H. M. Yoon, Y. Jung, S. C. Jun, S. Kondaraju, and J. S. Lee, “Molecular dynamics simulations of nanoscale and sub-nanoscale friction behavior between graphene and a silicon tip: analysis of tip apex motion.”, *Nanoscale* **7** **14**, 6295–303 (2015).
- ⁵⁸S. Li, Q. Li, R. W. Carpick, P. Gumbsch, X. Z. Liu, X. Ding, J. Sun, and J. Li, “The evolving quality of frictional contact with graphene”, *Nature* **539**, Number: 7630, 541–545 (2016).
- ⁵⁹A. Wijn, A. Fasolino, A. Filippov, and M. Urbakh, “Low friction and rotational dynamics of crystalline flakes in solid lubrication”, *Europhysics Letters (epl)* **95**, 10.1209/0295-5075/95/66002 (2011).
- ⁶⁰X. Feng, S. Kwon, J. Y. Park, and M. Salmeron, “Superlubric sliding of graphene nanoflakes on graphene”, *ACS Nano* **7**, Publisher: American Chemical Society, 1718–1724 (2013).
- ⁶¹F. Bonelli, N. Manini, E. Cadelano, and L. Colombo, “Atomistic simulations of the sliding friction of graphene flakes”, *The European Physical Journal B* **70**, 449–459 (2009).
- ⁶²M. Reguzzoni, A. Fasolino, E. Molinari, and M. C. Righi, “Friction by shear deformations in multilayer graphene”, *The Journal of Physical Chemistry C* **116**, 21104–21108 (2012).
- ⁶³Y. Liu, F. Grey, and Q. Zheng, “The high-speed sliding friction of graphene and novel routes to persistent superlubricity”, *Scientific Reports* **4**, 4875 (2014).
- ⁶⁴P. Zhu and R. Li, “Study of nanoscale friction behaviors of graphene on gold substrates using molecular dynamics”, *Nanoscale Research Letters* **13**, 34 (2018).
- ⁶⁵J. Zhang, E. Osloub, F. Siddiqui, W. Zhang, T. Ragab, and C. Basaran, “Anisotropy of graphene nanoflake–diamond interface frictional properties”, *Materials* **12**, 10.3390/ma12091425 (2019).
- ⁶⁶M. Reguzzoni and M. C. Righi, “Size dependence of static friction between solid clusters and substrates”, *Phys. Rev. B* **85**, 201412 (2012).
- ⁶⁷N. Varini, A. Vanossi, R. Guerra, D. Mandelli, R. Capozza, and E. Tosatti, “Static friction scaling of physisorbed islands: the key is in the edge”, *Nanoscale* **7**, 2093–2101 (2015).
- ⁶⁸R. Guerra, U. Tartaglino, A. Vanossi, and E. Tosatti, “Ballistic nanofriction”, *Nature Materials* **9**, 634–637 (2010).
- ⁶⁹U. D. Schwarz, O. Zwörner, P. Köster, and R. Wiesendanger, “Quantitative analysis of the frictional properties of solid materials at low loads. i. carbon compounds”, *Phys. Rev. B* **56**, 6987–6996 (1997).

- ⁷⁰J. Tersoff, “New empirical approach for the structure and energy of covalent systems”, *Phys. Rev. B* **37**, 6991–7000 (1988).
- ⁷¹Q. Zhang, D. Diao, and M. Kubo, “Nanoscratching of multi-layer graphene by molecular dynamics simulations”, *Tribology International* **88**, 85–88 (2015).
- ⁷²S. Corporation, *Pair-style lj/cut command*, (Dec. 22, 2022) https://docs.lammps.org/pair_lj.html.
- ⁷³X. Wang, S. Ramírez-Hinestrosa, J. Dobnikar, and D. Frenkel, “The lennard-jones potential: when (not) to use it”, *Phys. Chem. Chem. Phys.* **22**, 10624–10633 (2020).
- ⁷⁴R. Naeem, *Lennard-jones potential*, (Nov. 25, 2022) [https://chem.libretexts.org/Bookshelves/Physical_and_Theoretical_Chemistry_Textbook_Maps/Supplemental_Modules_\(Physical_and_Theoretical_Chemistry\)/Physical_Properties_of_Matter/Atomic_and_Molecular_Properties/Intermolecular_Forces/Specific_Interactions/Lennard-Jones_Potential](https://chem.libretexts.org/Bookshelves/Physical_and_Theoretical_Chemistry_Textbook_Maps/Supplemental_Modules_(Physical_and_Theoretical_Chemistry)/Physical_Properties_of_Matter/Atomic_and_Molecular_Properties/Intermolecular_Forces/Specific_Interactions/Lennard-Jones_Potential).
- ⁷⁵S. Corporation, *Pair-style sw command*, (Dec. 22, 2022) https://docs.lammps.org/pair_sw.html.
- ⁷⁶F. H. Stillinger and T. A. Weber, “Computer simulation of local order in condensed phases of silicon”, *Phys. Rev. B* **31**, 5262–5271 (1985).
- ⁷⁷S. Corporation, *Pair-style tersoff command*, (Dec. 22, 2022) https://docs.lammps.org/pair_tersoff.html.
- ⁷⁸T. Schneider and E. Stoll, “Molecular-dynamics study of a three-dimensional one-component model for distortive phase transitions”, *Phys. Rev. B* **17**, 1302–1322 (1978).